Research Square

Preprints are preliminary reports that have not undergone peer review.
They should not be considered conclusive, used to inform clinical practice,
or referenced by the media as validated information.

Exploration of the northern stratospheric polar vortex extremes via archetype analysis and tropospheric imprint

Dino Jeričević
MISU: Stockholms Universitet Meteorologiska institutionen
Abdel Hannachi
a.hannachi@misu.su.se

Stockholm University: Stockholms Universitet https://orcid.org/0000-0002-8255-5186
Didier P. Monselesan
CSIRO: Commonwealth Scientific and Industrial Research Organisation
Toshihiko Hirooka
Kyushu University: Kyushu Daigaku
Yuya Matsuyama
Kishocho Kisho Kenkyujo
James S. Risbey
CSIRO Alice Springs Laboratory: Commonwealth Scientific and Industrial Research Organisation
Chris C. Chapman
CSIRO Building Information Resource Centre: Commonwealth Scientific and Industrial Research Organisation

Research Article

Keywords: Stratospheric polar vortex, Sudden stratospheric warming, subseasonal to seasonal timescale, stratosphere-troposphere coupling

Posted Date: November 9th, 2026

DOI: https://doi.org/10.21203/rs.3.rs-11367588/v1

License: This work is licensed under a Creative Commons Attribution 4.0 International License.
Read Full License

Exploration of the northern stratospheric polar vortex extremes via archetype analysis and tropospheric imprint

Dino Jeričević[a], Abdel Hannachi[a,*], Didier P. Monselesan[b], Toshihiko Hirooka[c], Yuya Matsuyama[d], James S. Risbey[b], and Chris C. Chapman[b]

[a]Department of Meteorology and Bolin Centre for Climate Research, Stockholm University, Stockholm, Sweden

[b]CSIRO Environment, Hobart, Tasmania, Australia

[c]International Research Center for Space and Planetary Environmental Science, Kyushu University

[d]Fukuoka Regional Headquarters, Japan Meteorological Agency

October 11, 2026

(New revised version)

[0]*Corresponding author: Abdel Hannachi, abdel.hannachi@misu.su.se

Abstract

The winter stratospheric polar vortex is known to go through morphological change yielding various extreme states of its dynamic and thermodynamic state variables. These extreme states, including sudden stratospheric warming, generally have longer timescale compared to the chaotic limit of weather predictability, and may have significant impact on tropospheric variability. This offers the opportunity to boosting the predictability in the subseasonal-to-seasonal timescales especially regarding extreme events. Here extreme states of polar vortex are identified using archetypal analysis; a powerful unsupervised machine learning method. Polar vortex archetypes represent corners of the data convex hull and yield various extreme states including strong, split and displaced vortices. These states are shown to yield tropospheric and surface climate delayed response through teleconnections including North Atlantic Oscillation and Arctic Oscillation with lag of more than four to five weeks offering potential for predictability in the subseasonal-to-seasonal window.

Keywords: Stratospheric polar vortex, Sudden stratospheric warming, subseasonal to seasonal timescale, stratosphere-troposphere coupling.

1 Introduction

The study of extratropical climate variability and predictability is known to be a challenging topic due to the complex nonlinear processes involved and the interaction with other components of the atmosphere. One of those components, which we believe needs to be explored further, is the stratospheric polar vortex, e.g., Kidston et al. (2015). Stratospheric polar vortex is a region of low pressure rapidly rotating air around the winter poles. The stratospheric polar vortex – a band of strong westerlies resulting from the thermal wind (Holton and Hakim, 2013) – effectively blocks the polar air from interacting with lower latitude air mass.

The winter polar vortex is not in a permanent state of high potential vorticity (PV), but goes intermittently through dynamical changes resulting in amplitude variation and morphological deformation. These changes, resulting from eddy-mean flow interaction in the stratosphere, are driven by waves originating in the troposphere. Vertically propagating Rossby waves can break and interact with the polar vortex through dissipation and mixing (Charney and Drazin, 1961; Matsuno, 1971; Eliassen and Palm, 1961; McIntyre and Palmer, 1983) involving mainly perturbation of wavenumbers 1 and 2 and sometimes 3 (Finke et al., 2025) leading to the sudden stratospheric warming (SSW). This interaction can be represented by the Eliassen-Palm (E-P) flux, which is one of the diagnostic tools used to investigate wave activity affecting the polar vortex (Eliassen and Palm, 1961; Andrews and McIntyre, 1976; Edmon Jr et al., 1980).

SSW events represent extreme states of the polar vortex and consist of a sudden break down of the state of the vortex (Holton and Hakim, 2013; Butler et al., 2017) through rapid warming and/or zonal wind reversal. Rossby waves generated in the troposphere can propagate upward and amplify. In particular, strong Rossby waves generally associated with strong weather systems, including low pressure systems and blocking highs, can break upon reaching the stratosphere. This leads to the deceleration of the westerlies, and the induced residual circulation causes air to sink and warm adiabatically over the polar region. In fact, SSWs represent a dramatic change of the stratosphere through warming by several tens of degree Kelvin over a period of just a few days (Fig. 1), thus disrupting the temperature gradient between the mid-latitudes and the poles. In addition to changing the temperature gradient, winds also weaken and possibly reverse if the disruption is strong enough (Butler et al., 2017; Finke et al., 2025). During these events, noticeable deformation occurs in certain patterns that change the geometry and structure of the vortex, e.g. Hannachi et al. (2011). These states can be characterized as undisturbed, displaced and split states and can be described by the zonal wave number of the vortex state.

One of the benefits of analyzing the polar vortex and SSWs is that they have longer (than the synoptic)

timescales, and their impact on the troposphere is generally a slow process that may take up to one month or so to be felt at the Earth's surface. Due to these relatively long timescales, it is possible to gain insight into future weather even several weeks in advance. This gives us a potential for improving weather forecasts beyond the conventional predictability window of about 10 days. The gap between short term and long term weather forecast, the subseasonal-to-seasonal (S2S) range, is one of the most active areas of climate research today and the study of SSW events may provide an opportunity towards filling it.

There is a kind of consensus that knowledge of the stratospheric state can boost tropospheric predictability on S2S timescales and beyond (e.g., Butler et al. (2026)). Attempts to gain predictive power from the stratosphere started around two decades ago using simple statistical models, and found improved Northern Hemisphere extratropical surface skill at 10–45 days (e.g.Charlton et al. (2003); Christiansen (2005)). Persistence of lower-stratospheric anomalies associated with vortex dynamics enhances S2S predictability (e.g., Mariotti et al. (2020)). Extreme states of the winter stratospheric polar vortex have a tendency to be succeeded by anomalous near-surface circulation for several weeks, especially over the North Atlantic–Eurasia sector (Spaeth et al., 2024; Finke et al., 2023). For example, Spaeth et al. (2024) analyzed ensemble forecasts from the S2S database and found enhanced predictability during weak vortex conditions of negative North Atlantic Oscillation (NAO) in the ensemble mean with lead times of 2 to 5 weeks.

Mukougawa et al. (2009) found enhanced forecast skill for some prediction systems over Eurasia and Europe; see also Büeler et al. (2020) and Erner et al. (2022). Other examples of increased predictability at the surface following weak vortex events are observed over Eurasia with cold anomalies over Siberia, Scandinavia and Greenland, and warm anomalies over Alaska, north-eastern Canada North Africa/Middle East (Domeisen et al., 2020; Finke et al., 2023). Weak (e.g., SSWs) and strong vortex events tend to have opposite-signed effects on surface climate (Limpasuvan et al., 2005; Domeisen et al., 2020). According to Domeisen et al. (2020), strong polar vortex events tend to be followed by a positive NAO phase associated with increased risk of drought in the Mediterranean region. The weakening of the vortex following a SSW event can lead to cold air masses spilling into the midlatitudes and extratropics as the jet stream meanders, causing severe cold spells or persistent blocking over vast areas (Thompson et al., 2002; Kolstad et al., 2010; King et al., 2019; Finke et al., 2025).

Various possible mechanisms have been proposed for the stratospheric effect on the troposphere and consequent skillful S2S predictability following extreme states of the winter polar vortex. These include wave–mean flow interaction, wave reflection and absorption, and tropopause rising/dipping (e.g., Lang et al. (2020); Hannachi et al. (2025); Kidston et al. (2015)),which can affect teleconnection patterns such as the NAO and AO in the Northern Hemisphere, and also the Southern Annular Mode in the

Southern Hemisphere (e.g., Zi et al. (2025)). The stratosphere–troposphere interaction involves upward propagation of large-scale Rossby waves on approximately weekly timescales, accompanied by a delayed downward influence with timescales of up to about 6 weeks (e.g., Hartig et al. (2026); Mukhin et al. (2026); Finke et al. (2025)).

Out of all SSW events in the Northern Hemisphere, about two thirds impact surface weather and climate by shifting Atlantic jet equatorwards, leading to a negative NAO phase (e.g., Afargan-Gerstman and Domeisen (2020); Butler et al. (2017); Domeisen (2019)). Also, Afargan-Gerstman et al. (2020) show evidence of significant SSW events on North Atlantic marine cold outbreaks affecting the Nordic seas, i.e., Labrador, Norwegian, and Barents seas. The long time scale of the extreme SSW states can lead to extreme events, as in the case of "beast from the east" (Finke et al., 2025) helping towards extending surface extremes predictability.

Data-driven approaches, particularly machine learning, have recently spurred interest in weather forecasting and Earth science in general (e.g., Barnes et al. (2020); Beucler et al. (2021)). Few machine-learning algorithms have been applied to winter polar vortex dynamics because of the reduced sample size (Chen et al., 2024; de Fondeville et al., 2023). For example, Chen et al. (2024) applied an autoencoder neural network to a large ensemble of model simulations to study the phase portrait of vortex warming events, depicting a continuous transition of the vortex during warming events.

The weather and climate system is a high-dimensional complex system in which extreme events inherit this feature. Extreme events are traditionally analysed in terms of unidimensional time series (e.g., Fig. 1). Although the one-dimensional description is simple and easy to use, the polar vortex displays complex morphology that is not amenable to monitoring using a single zonal mean index. In addition to its complex spatial structure, the morphology of the polar vortex is also transient and characterized by complex evolution. In order to systematically investigate the polar vortex extreme states and their impact on surface climate the multivariate nature of those extremes has to be taken into account. A powerful and elegant way to address this is obtained through archetypal analysis (AA), an unsupervised machine learning method (Hannachi and Trendafilov, 2017; Chapman et al., 2025). Archetypes are extremes in the data state space, and are located on the vertices of the data convex hull, i.e. the data envelope (Cutler and Breiman, 1994), and for this reason AA is better suited to the complex morphology of the polar vortex states.

In this manuscript, we analyse the extreme states of the northern hemisphere winter polar vortex using archetypal analysis applied to the 850-K potential vorticity (PV), an excellent tracer for the polar vortex and SSW evolution. Tropospheric and surface effect of those extreme states are then investigated through composite analysis applied to thermodynamic and mass fields. The effect of wave activity is

also discussed. The manuscript is organised as follows. Section 2 presents the data and methodology. Section 3 discusses the archetypes of the winter polar vortex whereas section 4 investigates the impact on the troposphere and surface climate including the delayed effect with implications for predictability. A summary and discussion are given in the last section.

2 Data and Methodology

2.1 Data

The data are taken from the Japanese 55-year Reanalysis (JRA-55, Kobayashi et al. (2015)). The excerpt of Fig. 1 shows that the largest variability of 10-hPa zonal mean temperature is most prominent during November-March. Hence to analyse the northern winter evolution of the stratospheric polar vortex we consider (daily) November-March (NDJFM) period from 1958-11-01 to 2023-03-31. For convenience the 29th day of February in each leap year was discarded. In total, this makes 65 seasons, each lasting 151 days, i.e. 65×151 = 9815 days. Potential vorticity (PV) ($Km^2kg^{-1}s^{-1}$) on the 850-K isentrope is used here as a proxy of the the evolution of the stratospheric polar vortex.

The data are distributed on a regular grid with 1.25^o horizontal resolution over $20^oN - 90^oN$ yielding 57×288 lat-lon grid points. The daily (NDJFM) seasonal mean cycle is obtained by averaging, at each grid point, the values over the 65 years. Daily PV anomalies were calculated from the data by subtracting the daily seasonal cycle. To analyse the tropospheric and surface impact the following variables are considered: mean sea level pressure (MSLP), 2m-surface temperature, geopotential heights at 300- and 500-hPa, as well as zonal and meridional wind components at the same levels. Anomalous fields are computed similar to the PV anomalies.

2.2 Data dimension reduction

To reduce the dimensionality of the data and lower the computational cost, the Empirical Orthogonal Functions (EOF) method, also known as principal component analysis (PCA) (Hannachi, 2021) is applied. The EOFs/PCs of the space-time ($s \times t$) data matrix $\mathbf{X}_{s\times t}$ of PV anomalies are obtained using singular value decomposition (SVD):

$$\mathbf{X}_{s\times t} = \mathbf{U}\mathbf{\Lambda}\mathbf{V}^T \tag{1}$$

Here the matrix $\mathbf{U}$ contains all left singular vectors of $\mathbf{X}$, the matrix $\mathbf{V}$ represents all right singular vectors of $\mathbf{X}$ and the matrix $\mathbf{\Lambda}$ is a diagonal matrix with singular values sorted in decreasing order. Eq. (1) can be written as:

$$\begin{aligned} \mathbf{X}_{s\times t} \approx \mathbf{X}^r_{s\times t} &= \mathbf{U}_{s\times r}\,\mathbf{\Lambda}_{r\times r}\,\mathbf{V}^{\mathrm{T}}_{r\times t}, \\ &= \sum_{i=1}^{r} \lambda_i\,\mathrm{PC}_i(t)\,\mathrm{EOF}_i(s), \end{aligned} \tag{2}$$

where r is either the rank of the matrix $\mathbf{X}_{s\times t}$ or the number of EOFs/PCs retained. The EOFs and PCs represent respectively the columns of $\mathbf{U}_{s\times r}$ and $\mathbf{V}_{t\times r}$. Around 53 EOFs/PCs of the 850-K PV anomalies are needed for 95% explained variance, and the leading 60 EOFs/PCs are used in the remainder of the paper.

2.3 Archetypal analysis

Archetypal Analysis (AA) (Hannachi and Trendafilov, 2017), also known as the principal convex hull analysis (PCHA) method (Mørup and Hansen, 2012) is a unsupervised machine learning method, which looks for extreme states of the data in its state space by approximately identifying the vertices of the data convex hull. After applying the EOF/PCA method extreme states of the polar vortex are obtained via AA, applied to the EOFs/PCs of the 850-K PV anomalies. Basically, archetypes are obtained as convex combination $\mathbf{Z} = \mathbf{XC}$ of the data matrix $\mathbf{X}$, and $\mathbf{C}$ is a matrix of convex weights. In addition, the data are themselves approximated as convex combination $\mathbf{ZS}$ of the archetypes, i.e., $\mathbf{X} \approx \mathbf{ZS} = \mathbf{XCS}$.

We designate by $\mathbf{Z} = [\mathbf{z}_1, \dots \mathbf{z}_p]$ the matrix of p archetypes $\mathbf{z}_1, \dots \mathbf{z}_p$, then:salam

$$\mathbf{z}_k = \sum_{t=1}^{n} c_{tk}\mathbf{x}_t, \qquad k = 1, \dots p, \tag{3}$$

where $\mathbf{C} = (c_{tk})$ is the weight matrix and $\mathbf{x}_t$ is the anomaly data at time t. The weights are non-negative and add up to 1, giving it a probabilistic interpretation (Black et al., 2022), i.e.,

$$c_{tk} \geq 0 \quad \text{and} \quad \sum_{t=1}^{n} c_{tk} = 1 \qquad k = 1, \dots p. \tag{4}$$

In addition, the data themselves are convex combination of the archetypes, i.e. ,:

$$\mathbf{x}_t = \sum_{i=1}^{p} s_{it}\mathbf{z}_i, \qquad t = 1, \dots n, \tag{5}$$

$$s_{it} \geq 0; \quad \text{and} \quad \sum_{i=1}^{p} s_{it} = 1, \quad t = 1, \dots n, \tag{6}$$

with $\mathbf{S} = (s_{it})$ being another weight matrix.

Putting this altogether using the data matrix anomalies $\mathbf{X}$, the archetypes $\mathbf{Z} = \mathbf{XC}$ can be obtained through the following optimization problem:

$$\mathbf{Z} = [\mathbf{z}_1, \dots, \mathbf{z}_p], \quad \mathbf{S} = (s_{it}), \quad \text{and} \quad \mathbf{C} = (c_{ti}). \tag{7}$$

$$\min \left[\mathcal{RSS} = \|\mathbf{X} - \mathbf{XCS}\|_F^2 \right] \tag{8}$$

Here $\|\cdot\|_F^2$ is the Frobenius norm, that is $\|\mathbf{X}\|_F^2 = trace(\mathbf{XX^T})$. The square of the Frobenius norm between the AA representation and the original data corresponds to the Residual Sum of Squares (RSS). Various algorithms exist to solve the AA problem including the conventional 2-step algorithm (Cutler and Breiman, 1994), the autoencoder (Bauckhage et al., 2015), the manifold method (Hannachi and Trendafilov, 2017), and the dynamical system approach (e.g., Hannachi et al., 2026). Here we use the Breiman-Cutler algorithm, which boils down to an alternating constrained least-square (LS) problem:

- LS1: For fixed $\mathbf{C}$ obtain $\mathbf{Z}$ using Eq. (3), then determine $\mathbf{S}$ by minimizing $RSS = \|\mathbf{X} - \mathbf{ZS}\|_F^2$, i.e. Eq. (8).
- LS2: Compute $\mathbf{Z} = \mathbf{XS}^T(\mathbf{SS}^T)^{-1}$, then obtain $\mathbf{C}$ by minimizing $\|\mathbf{Z} - \mathbf{XC}\|_F^2$.
- LS3: Go to LS1 if the error is greater than a specified threshol or the number of iteration steps is reached.

We also denote by $\mathbf{Y} = [\mathbf{y}_1, \dots, \mathbf{y}_p] = \mathbf{X}\tilde{\mathbf{S}}^T$, which are patterns related to the archetypes $\mathbf{Z}$, to be discussed later, and $\tilde{\mathbf{S}}$ is the normalized $\mathbf{S}$ matrix. The property of the resulting weights, i.e., stochastic matrices (Eqs. 4 and 6), is very useful in modelling (e.g., Hannachi et al., 2026; Mukhin et al., 2025). In addition, it can be used to reduce the dimensionality of the system similar to EOF/PC analysis. Unlike EOFs/PCs, however, the archetypes do not necessarily nest (see section 3.2).

Geometrically, AA can be seen as representing the vertices of an approximate convex hull (envelope) that encompasses the dataset. The convex hull is the smallest convex set containing the data. A convex set is such a set that contains every possible line segment between any two elements. Figure 2 shows an illustration of a 2D dataset (red dots) with its convex hull (left panel) along with an approximate convex hull and archetypes (right panel), see also Hannachi and Trendafilov (2017).

The geometric interpretation is exemplified in Figure 3. The figure shows an illustrative example of archetypes using a three-dimensional (3D) Gaussian distribution (Fig. 3a) and a 3D uniform distribution (Fig. 3b). The archetypes of the 3D Gaussian distribution are uniformly distributed on the hull (or envelope) of the sample. On the other hand, the archetypes of the 3D uniform distribution are clustered in the corners (or vertices) of the rectangular parallelepiped representing the hull of the sample, see also Black et al. (2022). In order to consistently categorize the obtained archetypes, the 8 corners of the parallelepiped are given 8 colors, and each archetype is given the color of the closest corner. The last panel of Fig. 3 is discussed below.

3 Application to the stratospheric polar vortex

3.1 Polar vortex archetypes

Here we set out to explore and analyze the archetypes of the 850-K PV anomalies. The archetypes are computed using 60 PCs/EOFs of the PV anomalies, explaining more than 95% variance, by minimizing the RSS (Eq. 8) and exploring various values of the number of archetypes given by the hyperparameter p. The archetypes and the RSS decay are not very sensitive to changes in the number of EOFs/PCs explaining a reasonable amount of variance. Figure 4 shows the relative RSS versus the number p of archetypes chosen. The relative RSS is obtained by normalizing the RSS with the total variance of the dataset. The decrease of RSS is sharper for the first few archetypes, and then decreases slower for a higher number of archetypes. So, for example, for the first 5 archetypes, the relative RSS goes down to about 50%. In what follows we will analyze the first 8 archetypes, which decrease the RSS by about 60%. This choice is an approximate balance between accuracy and low-dimension selection. To help understand the distribution of archetypes of PV anomalies in state space, Figure 3c shows an illustration of the spread of 8 archetypes, from 400 different subsamples, using the leading 3 PCs, where the archetypes found for each subsample of 2000 points are colored based on the (Euclidean distance) proximity to the archetypes found for the full set of points corresponding to 9815 daily records. Unlike the Gaussian case (Figure 3a), Figure 3c illustrates well the clustering nature of these archetypes. Figure 3 points to an important observation, which differentiates the clustering nature of the extreme states of 850-K PV

anomalies from the Gaussian case. This is consistent with the fact that extremes in nature often occur in clusters, see (.e.g., Barton et al., 2022; Bonnafous and Lall, 2021). This particular topic is discussed in detail in another paper (Hannachi et al., 2026).

Using more archetypes usually makes the approximation more precise, but it also introduces the risk of redundancy due to the possibility of getting similar patterns. In addition, the computational demand increases while performing an analysis with a higher number of archetypes (Mørup and Hansen, 2012). Other alternatives can be used based, e.g., on the percentage of explained variance or the concept of hull clustering (Hannachi et al., 2026). Few diagnostic tools can be applied to get an appropriate value of p, such as the Gini coefficient (Black et al., 2022), or through analyzing the nesting property which is discussed below.

Figure 5 shows the map of the obtained eight archetypes. To ease interpretation and relate this to the illustration shown in Figure 2, the inside panel shows the projection of the archetypes (from 60 PCs) onto the leading two PCs, and where the gray small circles represent the PV anomaly projected onto PC1/PC2 plane. The 2D convex hull is shown by the outer contour. Note that the 2D convex hull (Fig. 5) has 12 vertices, or pure archetypes. Two-dimensional datasets are generally easy to identify their exact convex hull. But for 3 and higher dimensions, the convex hull becomes a difficult problem, and can only be approximated. With the 60 PCs, projection of the 8 archetypes, $\mathbf{Z} = \mathbf{XC}$, onto the leading (PC1, PC2) plane are shown by filled and color-coded circles connected by the inner contour lines, i.e. inner polygon.

Six out of the 8 archetypes are vertices of the inner solid contour line, and the other two are inside (Fig. 5). This is an artefact of the 2D projection of the high-dimensional (60 PCs) approximate convex hull. The colors in the inner panel represent data points closest to each of the 8 archetypes. The squares in the graph represent the patterns obtained as the product of the data by the (scaled) $\mathbf{S}$ matrix, $\mathbf{Y} = \mathbf{X}\tilde{\mathbf{S}}^T$, where $\tilde{S}_{ij} = S_{ij}/(\sum_k S_{ik})$ and $\sum_k \tilde{S}_{ik} = 1$. Each archetype from $\mathbf{XC}$ is linked to the associated pattern from $\mathbf{Y}$, via an arrow (Fig. 5), referred to as duals of archetypes $\mathbf{Z}$. These duals (not shown) bear resemblance to the associated archetypes but with smaller amplitude hence their proximity to the origin. We conjectured in Hannachi et al. (2026) that when the data are distributed near its boundary, the archetypes become close to their duals.

The 8 archetypes A1 to A8 reported in Figure 5 show different phases of the polar vortex. A splitting state can be seen in A1 and A2, where the polar vortex splits into two centers of high PV anomaly. In A1, two vortices occur over South Greenland and Siberia with the two centers of low PV over Canada and central Europe. Archetype A2 follows a similar pattern, but the two vortex centers are now located over North America. Archetypes A3 and A5 depict another common phenomenon of disrupted vortices,

showing vortex displacement. In A3, the vortex is displaced over the northwestern part of North America with a near circular structure. In the case of A5, the polar vortex is now displaced to the opposite side of the hemisphere, with clear stretching over northwestern Europe and northern Russia.

Two other types of less dramatic displacement are represented by A4 and A6. In A4, the polar vortex is slightly displaced over the northern north Atlantic, whereas A6 shows a slightly displaced vortex towards north eastern Russia and the Bering Strait. There are also some positive values outside its center with a slight band of less significant values stretching from its center over southern Europe. Note that the archetypes A3-A6, showing displaced polar vortex, might appear during the course of the split-type SSW evolution. The displaced vortex in the first stage may be quickly stretched and split into two centers, while the splitting polar vortex or two anticyclones may be merged into one center. A typical example will be shown later and discussed in Figure 7.

The last two archetypes, A7 and A8, represent nearly two opposite states of polar vortex. A7 represents approximately an undisturbed (normal) state of the polar vortex with (near uniform) high PV anomaly located over and around the pole. Note, however, that the vortex is not zonally symmetric over the pole, but has a stronger center slightly displaced off the pole and a weaker center over north Sweden. On the other hand, A8 represents approximately the opposite of A7, showing a weakened vortex with a negative PV anomaly over and around the pole. These eight archetypes capture reasonably well various possible extreme states of the polar vortex, namely, splitting, displacement, strong, and collapsed vortex states.

3.2 Temporal expression and nesting of archetypes

The archetype analysis yields the archetypes $\mathbf{Z}$ and two weight arrays $\mathbf{C}$ and $\mathbf{S}$ (e.g., Eq. (7)), shown in Figure 6. The $\mathbf{C}$ weights show how each individual data point contributes to the corresponding archetype. It is clearly visible that only a small number of data points effectively contribute to a given archetype. For example, if an archetype say $\mathbf{z}_{p_0}$ happens to be a data point vertex (at some time t_0) in the convex hull (see Fig. 1) then that archetype will have a unit weight associated with that observation and zero elsewhere. That is the corresponding $\mathbf{C}$ weights will be $c_{tp_0} = \delta_{tt_0}$, $t = 1, \ldots n$, where δ_{ij} is the Kronecker symbol.

The $\mathbf{S}$ weights are different in a sense that they are more continuous and tell us how much each archetype contributes to each data point, since in a given day the PV anomaly is obtained as convex combination of the different archetypes (see Eq. 5). So, each day has a particular weight from any given archetype, explaining the continuous nature of $\mathbf{S}$ matrix. A peak in a given archetype then shows the dominant role of the corresponding observation in that archetype. For example, if all archetypes contribute equally to a

given observation, then the **S** weights for that observation will be equal to 1/p. Note that in general large values of **C** yield large values of **S**. Figure 7 shows an example of the polar vortex states evolution during a SSW event in February 2018 (e.g., Harada et al. (2019)). Figure 6 shows that towards end January 2018 there is a large expression of archetype A4. In Early February the polar vortex is displaced and stretched over northern North Atlantic, north east Canada and northern Europe (Fig. 7). The stretching strengthens around 6 February, and splits soon after. The obtained two vortex centers detached and strengthened around 9-10 February, and peaked around 13 February. The vortices decay in the next two weeks and dissipate by the end of February. Linking the event to the archetypes, it can be seen that initially the vortex is connected to archetype A4, then gradually deforms and projects onto A2 around 13 February, see also the large **S** weight from A2 (Fig. 6), and dissipating finally into A8 around 19 February.

3.2.1 Archetype nesting

Archetypal analysis, unlike the EOF method, is not a linear optimization problem (e.g. eigenvalue problem as with EOF analysis), and one of the questions we discuss next is related to the issue of 'nesting'. EOF method, for example, is known to be nested in the sense that the leading p EOFs are a subset of the leading $p+1$ EOFs, etc.

Theoretically, nesting is not known to be a property of AA but in practice it is often satisfied for not very large cardinality p (Black et al., 2022; Chapman et al., 2025; Cutler and Breiman, 1994). Figure 8 shows the archetypes of PV anomalies for a number of cardinalities $p = 2, \ldots, 10$. To obtain matching between archetypes of different cardinality we use spatial correlation as measure of similarity. The figure clearly shows nesting up to p=10, and was also checked for up to p=20 (not shown). For quite larger values of p, nesting can become diffuse since we may get archetypes that are close to each other. Note that for $p = 2$, the obtained archetypes minimizing the RSS are aligned along the leading EOF of the data. The experiments suggest that nesting is stronger for larger slopes of the scree plot compared to the trailing (noisier) EOFs/PCs.

Now by examining, for example, the bottom left corner of Figure 8 it can be seen that for archetype 1 (Fig. 8) the pattern is consistent across different cardinalities (last row of Fig. 8), but becomes more intense with increasing cardinality. With more and more archetypes, the resulting patterns are better approximated and better capture the given data but at the expense of nesting. In other words, a balance has to be struck between the discriminating power of a reduced set of archetypes used for the detection of extreme states of the polar vortex and the level of approximation given by the AA representation of the original dataset.

3.2.2 Timescales of PV archetypes affiliation

The stratosphere evolves on different timescales, and it is of interest to be able to analyse this evolution, and we would like to capture, in particular, the flavor of both seasonality and interannual variability. The archetypes of the 850-K PV anomalies permit forming an event catalog portraying intraseasonal and interannual variability. Figure 9 displays a LEGO plot showing such an event catalog constructed from the **S** weights (Risbey et al., 2021; Chapman et al., 2025). From the **S** matrix we define, at each time t, the winning archetype q corresponding to the one maximizing (s_{it}), $i = 1, \ldots p$, i.e., $q = argmax(s_{it})$. The figure helps capture the seasonality (bottom subplot) and interannual variability (right subplot) with the main plot showing how the winning archetypes evolve with time. The figure also shows neatly how the winning archetypes can persist. Clearly, the different archetype affiliations have different characteristics of persistence and variability. Archetype 1, for example, is more frequent in the first part of the winter season compared to archetypes A3 or A6 (Fig. 9, bottom panel). Archetypes A4, A7, and A8 tend to occur somehow uniformly over the winter season. Weak stratospheric westerlies, in early winter, allows more wave-2 propagation in the stratosphere and this is more likely to yield stretching and splitting than displacement, which is more likely frequent starting mid-winter due to wave-1 propagation (Garfinkel et al., 2010; Domeisen et al., 2018; Mariaccia et al., 2022). Archetype A7, for example, reflects the regeneration of the vortex after each intermittent SSW event. Similarly, archetype A4 suggests a stretched state, looking like a final stage of a split or stretched vortex, and is likely to regenerate the vortex. Among all disturbed vortex states, the split vortex over North Russia and north-eastern North Atlantic (archetype A1) and the displaced vortex over Alaska (archetype A3) are more frequent, and the split vortex over Canada and eastern Russia (archetype A2) comes next.

Furthermore, the LEGO plot reflects varying long-term variability (Fig. 9, right panel). Archetype A6, for example, has long persistence, particularly in the early period and mid-1990s. Archetypes A1 and A2 suggest interdecadal variability with more occurrence in the mid 1980s and the recent two decades, plus occurrence in the mid 1970s late in the season. SSWs tend to be common during El-Nino with dominance of wave-1 and wave-2 during La-Nina (e.g., Palmeiro et al., 2023). Besides internal stratospheric variability, the strongest El-Nino events, e.g. in the late 1950's and early 1960's and also mid-1990's suggest a possible pathway to the persistence of the displaced vortex A6, and the occurrence of La-Nina events, e.g. in the mid-1980's possibly affect the vortex split A1 and A2. Nevertheless, most archetypes show large interannual and also decadal variability (Fig. 9, right panel). In fact, the LEGO plot reflects the complexity of vortex variability featuring persistence of, and transition between different states depending on the time of the year and season. Emerging particular transitions include $A3 \rightarrow A4 \rightarrow A6$ early 2010 and 1990 around mid-winter, $A1 \rightarrow A2$ around 2016 in addition to $A1 \rightarrow A2 \rightarrow A3$

around 1990 and alsalamso $A4 \rightarrow A6$ around mid-1980's.

3.3 Vortex extremes and eddy-mean flow forcing

Under specific conditions, lower boundary conditions in the northern hemisphere, including e.g., large-scale topography and variation in thermal forcing, excite quasi-stationary Rossby waves that propagate vertically (Charney and Drazin, 1961; Schoeberl and Newman, 2015) sometimes show the large wave transience (e.g., Holton and Hakim, 2013). Furthermore, they may break and dissipate when encountering critical layers (e.g. Matsuno, 1971). These drag processes deposit easterly momentum to the westerly flow (McIntyre and Palmer, 1983; Polvani and Waugh, 2004; Plumb, 1985). This results in perturbing and decelerating the polar vortex[1]. The wave activity in the stratosphere can be analyzed using three-dimensional wave activity flux, e.g. Plumb (1985), or the two-dimensional (latitude-height) Eliassen-Palm (EP) flux (Eliassen and Palm, 1961; Andrews and McIntyre, 1976). In this paper we use the latter for ease of plotting and interpretation, keeping in mind that in general the archetypes and the disturbed polar vortex are not zonally symmetric.

The wave drag resulting from the eddy-mean flow interaction can be evaluated by the divergence of the EP flux (Eliassen and Palm, 1961; Andrews and McIntyre, 1976) (meridional and vertical components):

$$\mathbf{F} = \begin{pmatrix} F_\phi \\ F_p \end{pmatrix} = a\cos\varphi \begin{pmatrix} -\overline{u'v'} \\ f\frac{\overline{v'\theta'}}{\partial\overline{\theta}/\partial p} \end{pmatrix} \tag{9}$$

where the overbar and prime refer respectively to the zonal mean and departure from it, f is the Coriolis parameter, θ is the potential temperature, φ is the latitude, a is the Earth's radius and (u, v) is the wind velocity. We note here that Eliassen and Palm (1961) actually made the pioneering work on this issue, while Andrews and McIntyre (1976) generalized it. Subsequently many studies on the middle atmosphere dynamics were based on Andrews and McIntyre (1976).

Here we explore the EP-flux and relationship with the extreme states of the polar vortex. Since the EP-flux divergence forces changes of zonal mean $\overline{u}$ (Holton and Hakim, 2013; Andrews and McIntyre, 1976) on short time scale (i.e., not seasonal timescale) we use the $\mathbf{C}$ matrix weight, i.e., the individual columns of $\mathbf{C}$ (all non-zero C-weights), to construct composites of EP-flux, associated with individual archetypes. Figure 10 shows the composites of $\mathbf{F}$ and its divergence corresponding to the archetypes of 850-K PV anomalies.

[1]Note that, actually, for the occurrence of SSWs wave transience (i.e., change of wave amplitude with time) and wave dissipation are very important (e.g., chapter 12 of Holton and Hakim, 2013). At least, at the beginning stage of SSWs, critical layers are not yet formed

The strongest convergence in the upper part of the domain roughly near 10-hPa/upward and around 60^oN is obtained with archetype A2, associated with strong vortex split (Fig. 5). The transition $A1 \rightarrow A2$ inferred from Fig. 9 suggests that the EP-flux convergence that forces A1 has increased and led to the splitted vortex A2. Next, we have convergence associated with archetype A3, associated with vortex displacement over Alaska (Fig. 5). There is also moderate convergence in the upper part of the domain, along with weak convergence at 10-hPa in the extratropics associated with archetype A4, also a displaced vortex. There is clear correspondence between the extreme vortex states, i.e. sudden stratospheric warming, with EP-flux convergence. Interestingly, archetype A6, a slightly displaced vortex, shows flux divergence centered at 3 hPa and 70^oN with downward propagation of $\mathbf{F}$. In fact, the EP-flux divergence of A6 (Fig. 10) suggests, along with the vortex state (Fig. 5), a downward reflection from the stratosphere due to a turning layer with a negative refractive index (e.g., Salby, 2012), associated with a cold event over Canada and Alaska (e.g., Kodera et al., 2016). Downward reflection events are preferred toward late winter (Feb-Mar) triggered by weakening of the stratospheric background westerlies (Wu et al., 2026). This provides support for the persistence of A6 during this time as can be seen in Fig. 9. On the other hand, Mukougawa et al. (2017) suggested that downward propagation of planetary waves is related to the barotropic instability inherent to the distorted polar vortex in the upper stratosphere associated with an SSW event in early March 2007. Hence, more studies are still needed on this issue. Furthermore, the weak vortex of archetype A8 shows flux divergence suggesting that the vortex has collapsed and may regenerate subsequently.

4 Vortex extreme states and tropospheric imprint

The impact of the stratospheric polar vortex on the troposphere and surface climate has been discussed in the literature and is still a hot research topic due to its importance in possibly extending the limits of predictability to S2S time scales. Here we discuss this topic based on vortex archetypes. Precisely, we investigate the influence of the stratospheric polar vortex on surface weather and climate through regression and composites of daily winter tropospheric variables with the normalized $\mathbf{S}$ weights. A number of anomalous fields are considered, including mean sea level pressure (MSLP) and surface temperature, in addition to geopotential height, zonal and meridional wind at 300 hPa and 500 hPa heights. But for convenience, we discuss below the result for MSLP and surface temperature, see the appendix for the other variables.

4.1 Contemporaneous MSLP and surface temperature response

In this section we discuss the contemporaneous impact of the polar vortex extreme states on MSLP and surface temperature anomalies. Figure 11 shows the regression coefficients for MSLP (first two columns) and surface temperature (last two columns) anomalies (response variable) with **S** weight matrix (predictor) of the archetypes, only 5% significant values are shown based in a student t-test. For each archetype the corresponding entire **S**-time series is used in the regression.

Clearly, different AA patterns correspond to different tropospheric imprints. Consider, for instance, the 1st and 2nd archetypes A1 and A2, representing a splitting vortex, but one is approximately a displaced pattern of the other. The MSLP response associated with the 1st archetype (Fig. 11) has three distinct positive anomaly centers sitting over eastern north Atlantic, western Russia, and north western Pacific, and three negative anomalies located respectively over Iceland, western Canada, and Siberia portraying a large scale wave number 3 pattern. The MSLP associated with the 2nd archetype A2 has three positive anomalies over Scandinavia, Alaska and western North Atlantic/eastern US coast, but also three negative anomaly centers mainly over Greenland, central Siberia and the central North Pacific. This map resembles a combination of a positive Scandinavian pattern (NOAA Climate Prediction Center, 2012b) with blocking over Scandinavia together in combination with a positive Pacific-North American (PNA) pattern (NOAA Climate Prediction Center, 2012a).

The strongest tropospheric response (Fig. 11) is obtained with the third archetype A3 (Fig. 5); a displaced vortex over northwestern America. The pressure response shows a tripole pattern with high pressure over the polar region and parts of the US, and two low pressure centers over central Europe and north Pacific. This response projects strongly onto the negative phase of AO, suggesting cold air outbreaks into the northern and central US and Europe. This is corroborated with the surface temperature plot in Figure 11 (third row), showing a strong response with a cold outbreak reaching down to several degrees Celsius below freezing in central US and northern Euroasia. At the same time, high temperature anomalies are observed in Greenland and the Far East. Note that the response to archetype A5, a displaced and stretched vortex over much of central Europe and the US, is approximately the opposite, but slightly weaker, than that of archetype A3, a projection onto the positive AO phase (Fig. 11), and similarly for the temperature response.

The opposite response pattern of surface temperature, but with a much weaker response magnitude, is obtained with the fifth archetype A5. Here, we have the opposite situation where now the vortex anomaly is displaced and stretched over much of central Europe and the US, and the associated anomalous MSLP response projects onto the positive AO. The signal of the anomalous temperature response in the

troposphere is higher than usual temperatures over most Eurasia and central US but with strength of up to 4°C, which is twice less than that of archetype A3.

In the case of archetypes A4 and A6, with the vortex displaced over northern North Atlantic and north of Alaska/Bering strait respectively (Fig. 5), one gets responses projecting respectively onto negative and positive NAO phase. In addition, for archetype A4 response (Fig. 11), there is one center of high MSLP anomaly around the pole stretching over central Russia, reminiscent of Siberian blocking. There is also a low pressure over the central Atlantic and eastern Pacific. The zonal wind response (appendix) indicates easterly winds in high latitudes and westerly winds over southern Europe, consistent with a negative NAO. The response to archetype A6 is, however, larger than that of archetype A4. Cold surface temperature anomalies are observed over northern Asia and Canada for archetypes A4 and A6, respectively.

The strong and "nearly" undisturbed vortex of archetype A7 (Fig. 5) yields a high pressure anomaly response over Scandinavia and main Europe with a low pressure over the pole (Fig. 11) projecting on the Scandinavian pattern which promotes blocking and dry conditions in northern Europe. The surface temperature response remains weak for this archetype. For archetype A8, corresponding to a collapsed vortex, the response shows a high pressure anomaly over Greenland extending to the pole and a negative band of pressure anomaly across Eurasia, Europe and northern North Atlantic, projecting on the negative NAO. The impact on the surface temperature shows a cooling over central Europe in consistency with Greenland blocking and the southward movement of cold Arctic air as the jet stream weakens and moves equatorwards, and also yield zonal wind reversal (Appendix).

We have also applied a composite analysis for both MSLP and surface temperature anomalies, by compositing over events corresponding to values of the weight **S** matrix greater than 0.5. The results reported in the appendix (Fig. A.1) are similar to Figure 11 but with a sharper contrast as would be expected. The response of the geopotential height, zonal and meridional wind at 300-hPa and 500-hPa are reported in Figures A.2, A.3 and A.4 respectively. In summary, the responses to various archetypes can be related sometimes, e.g. opposite phases, but can also be quite different due to the complex interaction between the polar vortex, large scale tropospheric (Rossby) waves and surface conditions.

4.2 Vortex state and tropospheric predictability

The previous section discusses the contemporaneous association or covariability between the extreme vortex state and surface climate. Here, we investigate the potential for any tropospheric predictive power by examining any delayed effect from the stratosphere (leading) on surface (lagging) climate. For

a given archetype, a lagged regression is computed between the corresponding **S** time series (Fig. 6) and the chosen gridded tropospheric or surface climate variable anomalies.

4.2.1 Delayed Response maps

Figure 12 shows the MSLP anomaly (lagged) response of the various archetypes A1 to A8 for various lags ranging from zero to 40 days. The lag zero is reproduced here for comparison with the remaining lags. For most archetypes, and as expected, the patterns weaken with increasing lag, with rates varying with archetypes. But, interestingly, for some archetypes the response remains unchanged and persists for large lags, and for two archetypes, the response even strengthens with lags. In particular, Archetype A7 response persists with its patterns strengthening until 30-40 day lag. More importantly, the anomalous MSLP response of Archetype A8 is highly persistent with the corresponding negative NAO pattern showing up even after 40 days lag, and the signal seems to get even stronger until around 32-day lag. Also, the response associated with archetype A6 (displaced vortex off the pole near the Bering strait, Fig. 5), particularly the low center over the polar region and Canada persists, until about 40 day lag. This MSLP response projects onto positive NAO but moves slightly eastward with longer lags. The response to the remaining archetypes A1, A3 and A4 persists for sometime up to about 3 weeks. Similar observations also apply to surface temperature anomalies as shown in Figure A.5 reported in the appendix.

4.2.2 Spatial correlation and amplitude changes

To complement the above analysis of the lagged response, we provide here a more quantitative description of those results by examining their spatial correlation and amplitudes as a function of lags. Figure 13 shows two measures, namely similarity and amplitude ratio as function of lags. The similarity measure is given here by the cosine of the angle, i.e. spatial correlation between the original (lag 0) map (Fig. 12, 1st column) and the subsequent lagged response maps (Fig. 12, remaining columns) for different archetypes. The shading shows the range of variability of the spatial correlation obtained by Monte-Carlo based on random shuffling. The theoretical 99% confidence interval is shown by the two (red) horizontal lines around the origin (mean) using a heuristic effective sample size $n^* = 410$) (see Appendix).

Figure 13 (top panels) shows clearly that all spatial correlations are quite large, well above the uncertainty range, and remain so for large lags, some of them well beyond a few months. This is the case, for example, of archetypes A6, A7 and A8 characterized by very slow decay. The response of archetypes A2, A4 and A5 (Fig. 13, top) have a long memory effect. The quite slow decrease of the response of archetypes A6, A7 and A8 (Fig. 13, top) is related to the long memory of the teleconnection patterns involving NAO, AO and PNA (see Figs. 11 and 12).

Precisely, the signal is most persistent for archetypes A6 and A8 where the values are maintained high around 0.9 for large lags. The correlation of the response to archetype A7 decreases quite slowly with increasing lag and remain above 0.75 for about 40-day lag. The response to archetype A5 drops to 0.3 in the first 3 weeks, but remains highly significant. The correlation of Archetype A1 response remains above 0.5 in the first 3 weeks then drops sharply afterwards. The response to archetype 2 (split vortex) drops in the first 2 weeks, but remains above 0.5 for up to 6 weeks. The above results clearly show that different states of the polar vortex yield different responses with different memories, and that the response persists for long lags.

Figure 13 (top) discusses the response pattern, with no mention of its amplitude. To address the latter Figure 13 (bottom panel) is similar to the spatial correlation shown in the top panels of Figure 13 but for amplitude ratio, that is the ratio of the magnitude of the response (considered as a vector in high-dimensional space), at a given lag, to that at lag-0. It is quite interesting to note that the amplitudes of the anomalous MSLP responses of archetypes A7 and A8 increase with lag up to about 4 weeks lag, and remain above unity for more than 6 weeks. The response to archetype A1 increases in amplitude reaching a maximum in about two weeks lag, and remains above unity for about 3 weeks lag. The remaining archetypal responses are smaller than unity, but some of them remain close to unity, such as the response to archetypes A2 and A6, for up to 5 week-lag.

5 Summary and discussion

Weather and climate extreme events, known for their impact on society, environment and the infrastructure on different levels, continue to hit us, and are expected to increase in a future climate. Atmospheric scientists have long been seeking to extend the limits of weather/climate predictability beyond the chaotic limit of about 10 days, in order to mitigate the impact of extremes. This led to the use of the bottom boundary conditions with long timescales, e.g. SST or sea ice, as predictors of the atmospheric state especially on S2S timescales. Another potential source of predictability comes from the stratosphere, characterized by its long timescales. The polar vortex, with its different extreme states, is known to persist for a long time, which can affect the troposphere and hence surface weather/climate with possible delay, offering potential for extending predictability limits. Here we have investigated the multivariate extreme states of the winter polar vortex of the NH using advanced unsupervised machine learning methods, namely archetypal analysis seeking vortex extremes, applied to 850-K PV anomaly of JRA-55. Given the complexity of the polar vortex and the clustered nature of its extreme states and, compared to methods existing in the literature, the novel AA approach provides a more consistent framework for the vortex complex morphology, dynamics and impacts than a single zonal mean index.

Eight archetypes have been identified reducing by 60% the residual sum of squares. Two archetypes represent split vortex center located over the North Atlantic/east Russia (archetype A1) and central Canada and Russia (archetype A2), respectively. Two archetypes represent vortex displaced center over western Canada (archetype A3) and the Bering Strait (archetype A6), and two other archetypes with displaced and stretched vortex over Northern Eurasia/North Atlantic (archetype A5) and Scandinavia/Southern US (archetype A4). The remaining two archetypes represent respectively, strong undisturbed (archetype A7) and collapsed (archetype A8) vortex. The archetypes have weights reflecting their time expression, which are used to identify their tropospheric effect.

Various responses are obtained depending on the extreme vortex state. Among the strongest responses, we found pattern projecting onto negative and positive AO, resulting respectively from the displaced vortex over northern Canada (archetype A3) and the stretched vortex over Northern Eurasia (archetype A5). The displaced and stretched vortex over Scandinavia/southern US (archetype A4) and the displaced vortex over the Bering Strait yield responses that project onto the positive and negative NAO phases, respectively. The collapsed vortex (archetype A8) also yields a response projecting onto the negative NAO phase. The two split vortex of archetypes A1 and A2 yield opposite phase responses with approximate zonal wave number 3. The strong vortex (archetype A7) yields a pattern projecting onto the positive AO with two high pressure centers over central Europe and north-east Pacific. The effect on surface temperature manifests especially with archetype A3 yielding low temperature anomalies reaching 6-8°C below freezing and also similar (but slightly less) temperature anomalies over Scandinavia and northern Eurasia. Archetype A2 also yields low temperature anomalies over Canada reaching around 5°C below freezing. Archetypes A1 and A4 yield moderate cold temperature anomalies over Eastern Russia and Northern Eurasia, respectively.

Predictability was also addressed by looking at the lagged effect on surface climate. We investigated both spatial correlation and response amplitude between the lagged and zero-lagged response. The response varies with archetypes where some responses show decrease of persistence whereas others show persistence for large lags of MSLP anomalies. Archetypes A8, A7, and A6 show great persistence reaching around 6 weeks lag. Archetypes A1, A3 and A4 persist for up to 3-4 weeks. This also applies to surface temperature anomalies to some extent. In addition to the long persistence the amplitude of the response shows an increase with lag for up to about 4 weeks and remains larger than unity for more than 7 weeks for archetypes A7 and A8, and more than 2 weeks for archetype A1. The other archetypes A2 and A6 amplitude ratio remains around 0.8 for up to 4 weeks.

The obtained results reveal the complex nature of tropospheric and surface response. It is known that the dominant response following SSWs projects onto negative NAO or negative northern annular mode, NAM (e.g., Baldwin and Dunkerton, 2001; Kidston et al., 2015; Butler et al., 2017, 2026). This projection is

to be expected as NAO/NAM are the dominant large scale modes of variability of northern extratropics. Nevertheless, examining the different obtained tropospheric responses shows some sort of non-uniformity among the different morphologies of the vortex extreme states due to complex interaction with surface processes. A -NAM stands out as a response to a displaced vortex over north west Canada and Alaska (A3). The splitted vortex, e.g., A2 or A1, has a weaker response compared to the displaced vortex (e.g. A3). This also applies to 2m temperature anomaly response. Some studies suggest that split vortex penetrates deeper into the lower stratosphere and has stronger surface impact compared to displaced vortex (e.g., Nakagawa and Yamazaki, 2006; Seviour et al., 2016). Our results does not suggest this is the case, see also, e.g., Maycock and Hitchcock (2015), White et al. (2019), and Chen et al. (2024). It is interesting to note here that tropospheric response to displaced vortex looks more consistent than that of split vortex. Occasional vortex strengthening in winter generally tends to have opposite effect to SSWs on surface, yielding responses projecting onto +NAO or +NAM (e.g., Domeisen et al., 2020) as is the case here with the MSLP anomaly response to A7, though with a weaker amplitude, or to A6. In terms of predictability, the downward influence of SSWs has a prolonged time scale ranging from a few weeks up to 2 months(Kidston et al., 2015; Domeisen et al., 2020; Davis et al., 2022), which are consistent with the obtained results here. The responses examined here have two features, persistence and amplitude. While persistence is observed to take place with several archetypes, noticeable amplitude increase with lag occurs with few archetypes and remain consistent for more than 6 weeks. Nevertheless, a more systematic analysis of the response to different vortex morphologies call for further inquiry, and can be investigated using a mechanistic model and controlled model experiment (e.g., Gerber and Polvani, 2009; Hitchcock and Simpson, 2014), a task that goes beyong the scope of the present paper.

Acknowledgements

CC, DPM and JSR acknowledge the support of the Australian Climate Service. TH acknowledges support from KAKENHI, Grant numbers JP20H01973 and JP25K07401.

Conflict of Interest

The authors declare no conflict of interest.

Data Availability Statement

The original data are JRA-55 and are generated from https://search.diasjp.net/en/dataset/JRA55. The transformed data are available from the corresponding author on reasonable request.

Open Research

The 850-K potential vorticity, the sea level pressure, the surface temperature, the 500-hPa geopotential

height and the wind field are provided by the Japanese Reanalyses (JRA-55) of the Japanese Meteorological Agency (JMA), and are available here https://search.diasjp.net/en/dataset/JRA55.

Appendix

Response of other variables

Figure A.1, shows the composites of MSLP and surface temperature anomalies over instances when the weight matrix **S** is greater than 0.5. The figure is comparable to Figure 11, except for the slight sharper contrast.

Figure A.2, shows regression coefficients for geopotential height at 300 hPa and 500 hPa with the **S** weight matrix for all eight archetypes. There is consistency between the 300- and 500-hPa height patterns. Archetypes A1, A2 and A3, and to some extent archetypes A5 and A6 yield stronger response, compared to the remaining ones. These patterns are also consistent with those obtained with MSLP anomalies (Fig. 11) concerning the location of highs and lows.

Figure A.3, is similar to Figure A.2, but for the zonal wind. For example, archetype A2 is dominated by increasing westerlies over the midlatitudes North Atlantic whereas archetype A3 is associated with increasing easterlies over the North Pacific.

Figure A.4, is similar to Figure A.3, but for the meridional wind. The patterns of the meridional wind are also consistent with the pressure patterns and also surface temperature anomalies. For instance, northerly wind anomaly for archetype A2 response explains the surface cooling over North America and parts of Siberia.

Finally we show here the lagged response of surface temperature. Figure A.5, is similar to Figure 12, but for surface temperature anomalies. It is interesting to note that similar observation from the MSLP anomalies response also apply to surface temperature anomalies to some extent.

Theoretical significance level for spatial correlation

In this appendix we develop a statistical test used in section 4.2.2 (Fig. 13, top) regarding the distribution of spatial correlations between patterns, i.e., scalar products between normalized vectors. Precisely, we consider here the cosine of the angle between patterns resulting from the scalar product between (normalised) patterns, i.e. vectors on the unit hypersphere S_{n-1} (of dimension $n-1$, also referred to as $(n-1)$-sphere) in n-dimensional space $\mathbb{R}^n$.

In this context it is convenient to consider spherical coordinates where the coordinates $\mathbf{x} = (x_1, \dots x_n)^T$ are transformed into $(r, \theta_1, \dots, \theta_{n-1})^T$, with $r \geq 0$, $-\frac{\pi}{2} \leq \theta_k \leq \frac{\pi}{2}$ $(1 \leq k \leq n-2)$, and $0 \leq \theta_{n-1} \leq 2\pi$,

see e.g., Hannachi (2021, page 5). Note that the area of S_{n-1} is $2\frac{\pi^{\frac{n}{2}}}{\Gamma(\frac{n}{2})}$. The correlation measure used in section 4.2.2 compares the different responses to SSW events (at different lags) with a given pattern (the response at zero-lag). Therefore we consider here a fixed direction, or equivalently a point on the hypersphere S_{n-1}, given for example by the first axis (parametrized by θ_1). The probability distribution of the angle θ_1 between a randomly chosen (unit) vector (or point on S_{n-1}) and the fixed direction is obtained by integrating the area element over the remaining spherical coordinates. This probability density function $f()$ is proportional to:

$$f(\theta_1) \propto 2\pi \sin^{n-2}\theta_1 \int_0^\pi \dots \int_0^\pi \sin^{n-3}\theta_2 \dots \sin^2\theta_{n-3} \sin\theta_{n-2} d\theta_2 \dots d\theta_{n-2} \tag{A1}$$

Recalling that $\int_0^\pi sin^m\theta d\theta = \frac{\Gamma(\frac{1}{2})\Gamma(\frac{m+1}{2})}{\Gamma(\frac{m+2}{2})}$, the pdf becomes (after scaling by the area of the hypersphere):

$$f(\theta_1) = \frac{\sin^{n-2}\theta_1 \Gamma(\frac{n}{2})}{\Gamma(\frac{1}{2})\Gamma(\frac{n-1}{2})} = \frac{\sin^{n-2}\theta_1}{B(\frac{1}{2}, \frac{n-1}{2})} \tag{A2}$$

where $\Gamma()$ and $B()$ are respectively the gamma and beta functions (e.g., (Davis, 1972)).

Next, we make use of the property of variable changes, namely, if X is a random variable with pdf $f(x)$ then the pdf $g(y)$ of the new random variable $Y = h(X)$, with $h()$ being monotonically increasing function is

$$g(y) = f\left(h^{-1}(y)\right) \frac{d}{dy}\left(h^{-1}(y)\right) \tag{A3}$$

Note that if $h()$ is monotonically decreasing the above expression is multiplied by -1.

Applying Eq (A3) to Eq (A2) using $h(x) = \cos x$, with $0 \le x \le \pi$, the pdf of $Y = \cos\theta_1$ reads:

$$g(y) = \frac{(1-y^2)^{\frac{n-3}{2}}}{B(\frac{1}{2}, \frac{n-1}{2})}, \quad -1 \le y \le 1. \tag{A4}$$

The variance σ^2 of the above distribution is:

$$\sigma^2 = \frac{2}{B(\frac{1}{2}, \frac{n-1}{2})} \int_0^1 y^2 (1-y^2)^{\frac{n-3}{2}} dy = \frac{B(\frac{3}{2}, \frac{n-1}{2})}{B(\frac{1}{2}, \frac{n-1}{2})}, \tag{A5}$$

that is $\sigma^2 = n^{-1}$, which is used to compute the confidence interval of the obtained spatial correlation. Note that n represents the dimension of the map, i.e. the number of grid points. To account for the spatial autocorrelation we inflate the variance using an effective sample size n^* obtained by considering heuristically grid size of 5° in latitude and 12.5^o in longitude yielding $n^* = 410$.

References

Afargan-Gerstman, H. and Domeisen, D. I. (2020). Pacific modulation of the north atlantic storm track response to sudden stratospheric warming events. *Geophysical Research Letters*, 47(2):e2019GL085007.

Afargan-Gerstman, H., Polkova, I., Papritz, L., Ruggieri, P., King, M. P., Athanasiadis, P. J., Baehr, J., and Domeisen, D. I. (2020). Stratospheric influence on north atlantic marine cold air outbreaks following sudden stratospheric warming events. *Weather and Climate Dynamics*, 1(2):541.

Andrews, D. G. and McIntyre, M. E. (1976). Planetary Waves in Horizontal and Vertical Shear: The Generalized Eliassen-Palm Relation and the Mean Zonal Acceleration. *Journal of the Atmospheric Sciences*, 33(11):2031–2048. Publisher: American Meteorological Society Section: Journal of the Atmospheric Sciences.

Baldwin, M. P. and Dunkerton, T. J. (2001). Stratospheric harbingers of anomalous weather regimes. *Science*, 294(5542):581–584.

Barnes, E. A., Toms, B., Hurrell, J. W., Ebert-Uphoff, I., Anderson, C., and Anderson, D. (2020). Indicator patterns of forced change learned by an artificial neural network. *Journal of Advances in Modeling Earth Systems*, 12(9):e2020MS002195.

Barton, Y., Rivoire, P., Koh, J., Kopp, J., Martius, O., et al. (2022). On the temporal clustering of european extreme precipitation events and its relationship to persistent and transient large-scale atmospheric drivers. *Weather and Climate Extremes*, 38:100518.

Bauckhage, C., Kersting, K., Hoppe, F., and Thurau, C. (2015). Archetypal analysis as an autoencoder. In *Workshop New Challenges in Neural Computation*, volume 2015, pages 8–16. Citeseer.

Beucler, T., Ebert-Uphoff, I., Rasp, S., Pritchard, M., and Gentine, P. (2021). Machine learning for clouds and climate (invited chapter for the agu geophysical monograph series "clouds and climate").

Black, A. S., Monselesan, D. P., Risbey, J. S., Sloyan, B. M., Chapman, C. C., Hannachi, A., Richardson, D., Squire, D. T., Tozer, C. R., and Trendafilov, N. (2022). Archetypal analysis of geophysical data illustrated by sea surface temperature. *Artificial Intelligence for the Earth Systems*, 1(3):e210007.

Bonnafous, L. and Lall, U. (2021). Space-time clustering of climate extremes amplify global climate impacts, leading to fat-tailed risk. *Natural Hazards and Earth System Sciences*, 21(8):2277–2284.

Büeler, D., Beerli, R., Wernli, H., and Grams, C. M. (2020). Stratospheric influence on ecmwf sub-seasonal forecast skill for energy-industry-relevant surface weather in european countries. *Quarterly Journal of the Royal Meteorological Society*, 146(733):3675–3694.

Butler, A. H., Charlton-Perez, A., Domeisen, D. I., Garfinkel, C. I., Gerber, E. P., Hitchcock, P., Karpechko, A. Y., Maycock, A. C., Son, S.-W., and Thompson, C. (2026). Subseasonal predictability and the stratosphere. In *Sub-seasonal to seasonal prediction*, pages 355–397. Elsevier.

Butler, A. H., Sjoberg, J. P., Seidel, D. J., and Rosenlof, K. H. (2017). A sudden stratospheric warming compendium. *Earth System Science Data*, 9(1):63–76.

Chapman, C. C., Monselesan, D. P., Risbey, J. S., Hannachi, A., Lucarini, V., and Matear, R. (2025). The typicality of regimes associated with northern hemisphere heatwaves. *Journal of Climate*.

Charlton, A. J., O'Neill, A., Stephenson, D., Lahoz, W., and Baldwin, M. (2003). Can knowledge of the state of the stratosphere be used to improve statistical forecasts of the troposphere? *Quarterly Journal of the Royal Meteorological Society: A journal of the atmospheric sciences, applied meteorology and physical oceanography*, 129(595):3205–3224.

Charney, J. G. and Drazin, P. G. (1961). Propagation of planetary-scale disturbances from the lower into the upper atmosphere. *Journal of Geophysical Research*, 66(1):83–109.

Chen, Y.-C., Liang, Y.-C., Wu, C.-M., Huang, J.-D., Lee, S. H., Wang, Y., and Zeng, Y.-J. (2024). Exploiting a variational auto-encoder to represent the evolution of sudden stratospheric warmings. *Environmental Research: Climate*, 3(2):025006.

Christiansen, B. (2005). Downward propagation and statistical forecast of the near-surface weather. *Journal of Geophysical Research: Atmospheres*, 110(D14).

Cutler, A. and Breiman, L. (1994). Archetypal analysis. *Technometrics*, 36(4):338–347.

Davis, N., Richter, J., Glanville, A., Edwards, J., and LaJoie, E. (2022). Limited surface impacts of the january 2021 sudden stratospheric warming. *Nature communications*, 13(1):1136.

Davis, P. J. (1972). Gamma function and related functions. *Handbook of mathematical functions*, 256.

de Fondeville, R., Wu, Z., Székely, E., Obozinski, G., and Domeisen, D. I. (2023). Improved extended-range prediction of persistent stratospheric perturbations using machine learning. *Weather and Climate Dynamics*, 4(2):287–307.

Domeisen, D. I. (2019). Estimating the frequency of sudden stratospheric warming events from surface observations of the north atlantic oscillation. *Journal of Geophysical Research: Atmospheres*, 124(6):3180–3194.

Domeisen, D. I., Butler, A. H., Charlton-Perez, A. J., Ayarzagüena, B., Baldwin, M. P., Dunn-Sigouin, E., Furtado, J. C., Garfinkel, C. I., Hitchcock, P., Karpechko, A. Y., et al. (2020). The role of the

stratosphere in subseasonal to seasonal prediction: 1. predictability of the stratosphere. *Journal of Geophysical Research: Atmospheres*, 125(2):e2019JD030920.

Domeisen, D. I., Martius, O., and Jiménez-Esteve, B. (2018). Rossby wave propagation into the northern hemisphere stratosphere: The role of zonal phase speed. *Geophysical Research Letters*, 45(4):2064–2071.

Edmon Jr, H., Hoskins, B., and McIntyre, M. (1980). Eliassen-palm cross sections for the troposphere. *Journal of Atmospheric Sciences*, 37(12):2600–2616.

Eliassen, A. and Palm, E. (1961). On the transfer of energy in stationary mountain waves. *Geofys. Publ.*, 22:1–23.

Erner, I., Karpechko, A., Kämäräinen, M., and Järvinen, H. (2022). Stratosphere–troposphere coupling enhances subseasonal predictability of northern eurasian cold spells. *Quarterly Journal of the Royal Meteorological Society*, 148(747):2769–2783.

Finke, K., Hannachi, A., and Hirooka, T. (2023). Exceptionally persistent eurasian cold events and their stratospheric link. *Asia-Pacific Journal of Atmospheric Sciences*, 59(1):95–111.

Finke, K., Hannachi, A., Hirooka, T., Matsuyama, Y., and Iqbal, W. (2025). The stratospheric polar vortex and surface effects: The case of the north american 2018/19 cold winter. *Atmosphere*, 16(4):445.

Garfinkel, C. I., Hartmann, D. L., and Sassi, F. (2010). Tropospheric precursors of anomalous northern hemisphere stratospheric polar vortices. *Journal of Climate*, 23(12):3282–3299.

Gerber, E. P. and Polvani, L. M. (2009). Stratosphere–troposphere coupling in a relatively simple agcm: The importance of stratospheric variability. *Journal of Climate*, 22(8):1920–1933.

Hannachi, A. (2021). *Patterns identification and data mining in weather and climate*, volume 10. Springer.

Hannachi, A., Finke, K., Trendafilov, N., Monselesan, D., Risbey, J., Chapman, C., and Chafik, L. (2026). Weather and climate extremes: Simplex, dynamical systems and hull clustering. *Journal of Geophysical Research: Atmospheres*, 131(4):e2025JD045044.

Hannachi, A., Lechner, M., Finke, K., and Mukhin, D. (2025). Stratospheric polar vortex, wave absorption/reflection and effect on surface climate. *Climate Dynamics*, 63(2):126.

Hannachi, A., Mitchell, D., Gray, L., and Charlton-Perez, A. (2011). On the use of geometric moments to examine the continuum of sudden stratospheric warmings. *Journal of the Atmospheric Sciences*, 68(3):657–674.

Hannachi, A. and Trendafilov, N. (2017). Archetypal analysis: Mining weather and climate extremes. *Journal of Climate*, 30(17):6927–6944.

Harada, Y., Sato, K., Kinoshita, T., Yasui, R., Hirooka, T., and Naoe, H. (2019). Diagnostics of a WN2-Type Major Sudden Stratospheric Warming Event in February 2018 Using a New Three-Dimensional Wave Activity Flux. *Journal of Geophysical Research: Atmospheres*, 124(12):6120–6142. _eprint: https://agupubs.onlinelibrary.wiley.com/doi/pdf/10.1029/2018JD030162.

Hartig, K., Harnik, N., and Tziperman, E. (2026). Identifying time scales and spatial patterns of upward and downward influences between the wintertime troposphere and stratosphere. *Journal of Climate*, 39(13):3885–3904.

Hitchcock, P. and Simpson, I. R. (2014). The downward influence of stratospheric sudden warmings. *Journal of the Atmospheric Sciences*, 71(10):3856–3876.

Holton, J. R. and Hakim, G. J. (2013). *An Introduction to Dynamic Meteorology*, volume 88. Academic Press, Burlington, MA, 5 edition.

Kidston, J., Scaife, A. A., Hardiman, S. C., Mitchell, D. M., Butchart, N., Baldwin, M. P., and Gray, L. J. (2015). Stratospheric influence on tropospheric jet streams, storm tracks and surface weather. *Nature Geoscience*, 8(6):433–440.

King, A. D., Butler, A. H., Jucker, M., Earl, N. O., and Rudeva, I. (2019). Observed relationships between sudden stratospheric warmings and european climate extremes. *Journal of Geophysical Research: Atmospheres*, 124(24):13943–13961.

Kobayashi, S., Ota, Y., Harada, Y., Ebita, A., Moriya, M., Onoda, H., Onogi, K., Kamahori, H., Kobayashi, C., Endo, H., Miyaoka, K., and Takahashi, K. (2015). The JRA-55 reanalysis: General specifications and basic characteristics. *J. Met. Soc. Japan*, 93(1):5–48.

Kodera, K., Mukougawa, H., Maury, P., Ueda, M., and Claud, C. (2016). Absorbing and reflecting sudden stratospheric warming events and their relationship with tropospheric circulation. *Journal of Geophysical Research: Atmospheres*, 121(1):80–94.

Kolstad, E. W., Breiteig, T., and Scaife, A. A. (2010). The association between stratospheric weak polar vortex events and cold air outbreaks in the northern hemisphere. *Quarterly Journal of the Royal Meteorological Society*, 136(649):886–893.

Lang, A. L., Pegion, K., and Barnes, E. A. (2020). Introduction to special collection:"bridging weather and climate: subseasonal-to-seasonal (s2s) prediction". *Journal of Geophysical Research: Atmospheres*, 125(4):e2019JD031833.

765 Limpasuvan, V., Hartmann, D. L., Thompson, D. W., Jeev, K., and Yung, Y. L. (2005). Stratosphere-
766 troposphere evolution during polar vortex intensification. *Journal of Geophysical Research: Atmo-*
767 *spheres*, 110(D24).

768 Mariaccia, A., Keckhut, P., and Hauchecorne, A. (2022). Classification of stratosphere winter evolutions
769 into four different scenarios in the northern hemisphere. *Journal of Geophysical Research: Atmospheres*,
770 127(13):e2022JD036662.

771 Mariotti, A., Baggett, C., Barnes, E. A., Becker, E., Butler, A., Collins, D. C., Dirmeyer, P. A., Ferranti,
772 L., Johnson, N. C., Jones, J., et al. (2020). Windows of opportunity for skillful forecasts subseasonal
773 to seasonal and beyond. *Bulletin of the American Meteorological Society*, 101(5):E608–E625.

774 Matsuno, T. (1971). A dynamical model of the stratospheric sudden warming. *Journal of Atmospheric*
775 *Sciences*, 28(8):1479–1494.

776 Maycock, A. C. and Hitchcock, P. (2015). Do split and displacement sudden stratospheric warmings
777 have different annular mode signatures? *Geophysical Research Letters*, 42(24):10–943.

778 McIntyre, M. E. and Palmer, T. (1983). Breaking planetary waves in the stratosphere. *Nature*,
779 305(5935):593–600.

780 Mørup, M. and Hansen, L. K. (2012). Archetypal analysis for machine learning and data mining.
781 *Neurocomputing*, 80:54–63.

782 Mukhin, D., Samoilov, R., and Hannachi, A. (2025). Metastability and teleconnection of atmospheric
783 circulation via hidden markov models and network modularity. *Scientific Reports*, 15(1):1–16.

784 Mukhin, D., Samoilov, R., Hannachi, A., and Feigin, A. (2026). Revealing stratosphere-troposphere
785 interactions via regime-based transfer entropy. *Nonlinear Dynamics*. Under revision.

786 Mukougawa, H., Hirooka, T., and Kuroda, Y. (2009). Influence of stratospheric circulation on the
787 predictability of the tropospheric northern annular mode. *Geophysical Research Letters*, 36(8).

788 Mukougawa, H., Noguchi, S., Kuroda, Y., Mizuta, R., and Kodera, K. (2017). Dynamics and Predictabil-
789 ity of Downward-Propagating Stratospheric Planetary Waves Observed in March 2007. *Journal of the*
790 *Atmospheric Sciences*, 74(11):3533–3550. Publisher: American Meteorological Society Section: Jour-
791 nal of the Atmospheric Sciences.

792 Nakagawa, K. I. and Yamazaki, K. (2006). What kind of stratospheric sudden warming propagates to
793 the troposphere? *Geophysical research letters*, 33(4).

794 NOAA Climate Prediction Center (2012a). Pacific/north american (pna) teleconnection pattern. `https:`
795 `//www.cpc.ncep.noaa.gov/data/teledoc/pna.shtml`. Accessed: 2025-05-30.

NOAA Climate Prediction Center (2012b). Scandinavia (scand) teleconnection pattern. https://www.cpc.ncep.noaa.gov/data/teledoc/scand.shtml. Accessed: 2025-05-30.

Palmeiro, F., García-Serrano, J., Ruggieri, P., Batté, L., and Gualdi, S. (2023). On the influence of enso on sudden stratospheric warmings. *Journal of Geophysical Research: Atmospheres*, 128(8):e2022JD037607.

Plumb, R. A. (1985). On the three-dimensional propagation of stationary waves. *Journal of Atmospheric Sciences*, 42(3):217–229.

Polvani, L. M. and Waugh, D. W. (2004). Upward wave activity flux as a precursor to extreme stratospheric events and subsequent anomalous surface weather regimes. *Journal of climate*, 17(18):3548–3554.

Risbey, J. S., Monselesan, D. P., Black, A. S., Moore, T. S., Richardson, D., Squire, D. T., and Tozer, C. R. (2021). The identification of long-lived southern hemisphere flow events using archetypes and principal components. *Monthly Weather Review*, 149(6):1987–2010.

Salby, M. L. (2012). *Physics of the Atmosphere and Climate*. Cambridge University Press.

Schoeberl, M. and Newman, P. (2015). Middle atmosphere| polar vortex. *Encyclopedia of atmospheric sciences*, pages 12–17.

Seviour, W. J., Gray, L. J., and Mitchell, D. M. (2016). Stratospheric polar vortex splits and displacements in the high-top cmip5 climate models. *Journal of Geophysical Research: Atmospheres*, 121(4):1400–1413.

Spaeth, J., Rupp, P., Garny, H., and Birner, T. (2024). Stratospheric impact on subseasonal forecast uncertainty in the northern extratropics. *Communications Earth & Environment*, 5(1):126.

Thompson, D. W., Baldwin, M. P., and Wallace, J. M. (2002). Stratospheric connection to northern hemisphere wintertime weather: Implications for prediction. *Journal of Climate*, 15(12):1421–1428.

White, I., Garfinkel, C. I., Gerber, E. P., Jucker, M., Aquila, V., and Oman, L. D. (2019). The downward influence of sudden stratospheric warmings: Association with tropospheric precursors. *Journal of Climate*, 32(1):85–108.

Wu, F., Tan, X., Wang, W., Deng, Q., Zhao, S., and Zhang, Z. (2026). A novel index for regional stratospheric wave reflection and its impact on surface air temperature over north america. *Atmospheric and Oceanic Science Letters*, page 100859.

Zi, Y., Long, Z., Sheng, J., Lu, G., Perrie, W., and Xiao, Z. (2025). The sudden stratospheric warming events in the antarctic in 2024. *Geophysical Research Letters*, 52(7):e2025GL115257.

Figure captions

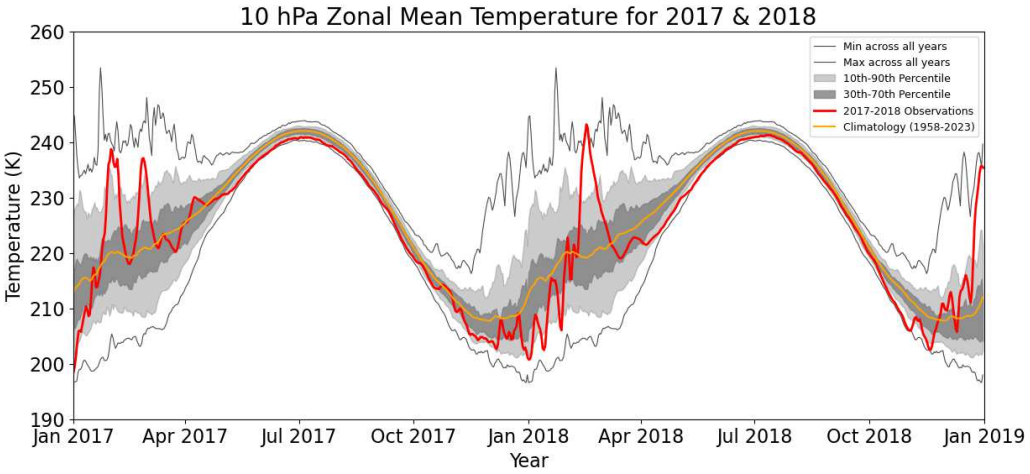

Figure 1: Zonal mean temperature at the 10 hPa level during 2017–2019. Also shown are the minimum, maximum, climatology, and various percentiles over all years, averaged over latitudes 65°–90°N. The corresponding state of the polar vortex during winter 2018 is discussed later (Fig. 7)

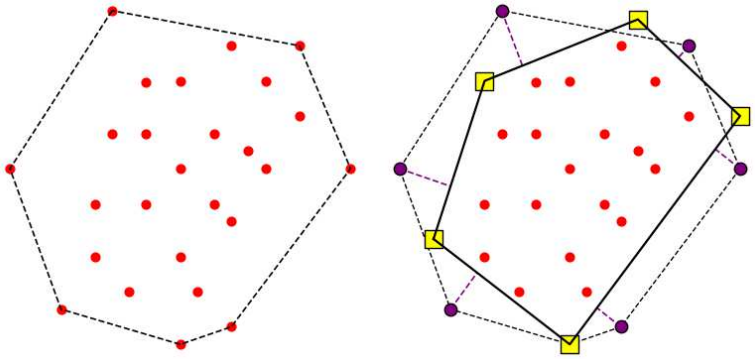

Figure 2: Illustration of a 2D data set (red dots) with its convex hull shown by a dashed line (left), and an approximate convex hull shown by a continuous line along with archetypes shown by yellow squares (right).

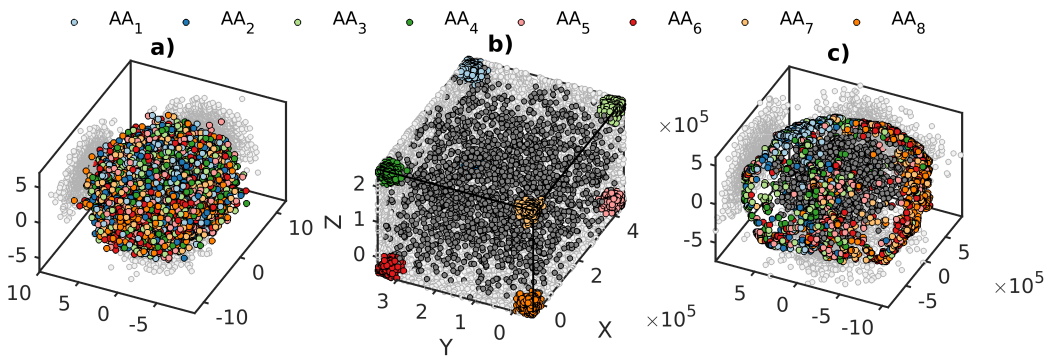

Figure 3: AA results for cardinality 8 performed on 3D multivariate normal distribution distribution (a), rectangular uniform distribution (b) and the first 3 PCs of 850-K PV anomalies (c). AA is applied to 400 sets of 2000 points randomly selected from the first 3 PCs scaled by respective eigenvalues. The last set of points out of the 400 chosen are shown in dark gray and the resulting archetypes for all 400 trials in the colors indicated by the legend. Color attribution is based on proximity to both the parallelepiped corners (b) and to the archetypes found for the full 3 PCs pointset (c), see text for details.

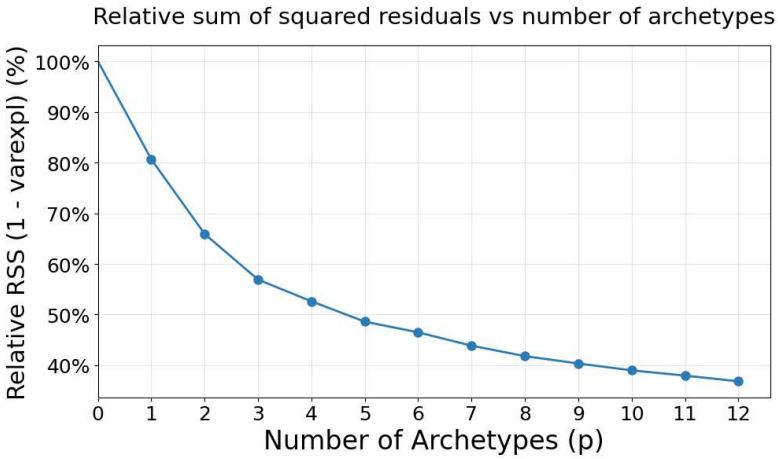

Figure 4: Relative sum of squared residuals (RSS) vs the number p of archetypes chosen.

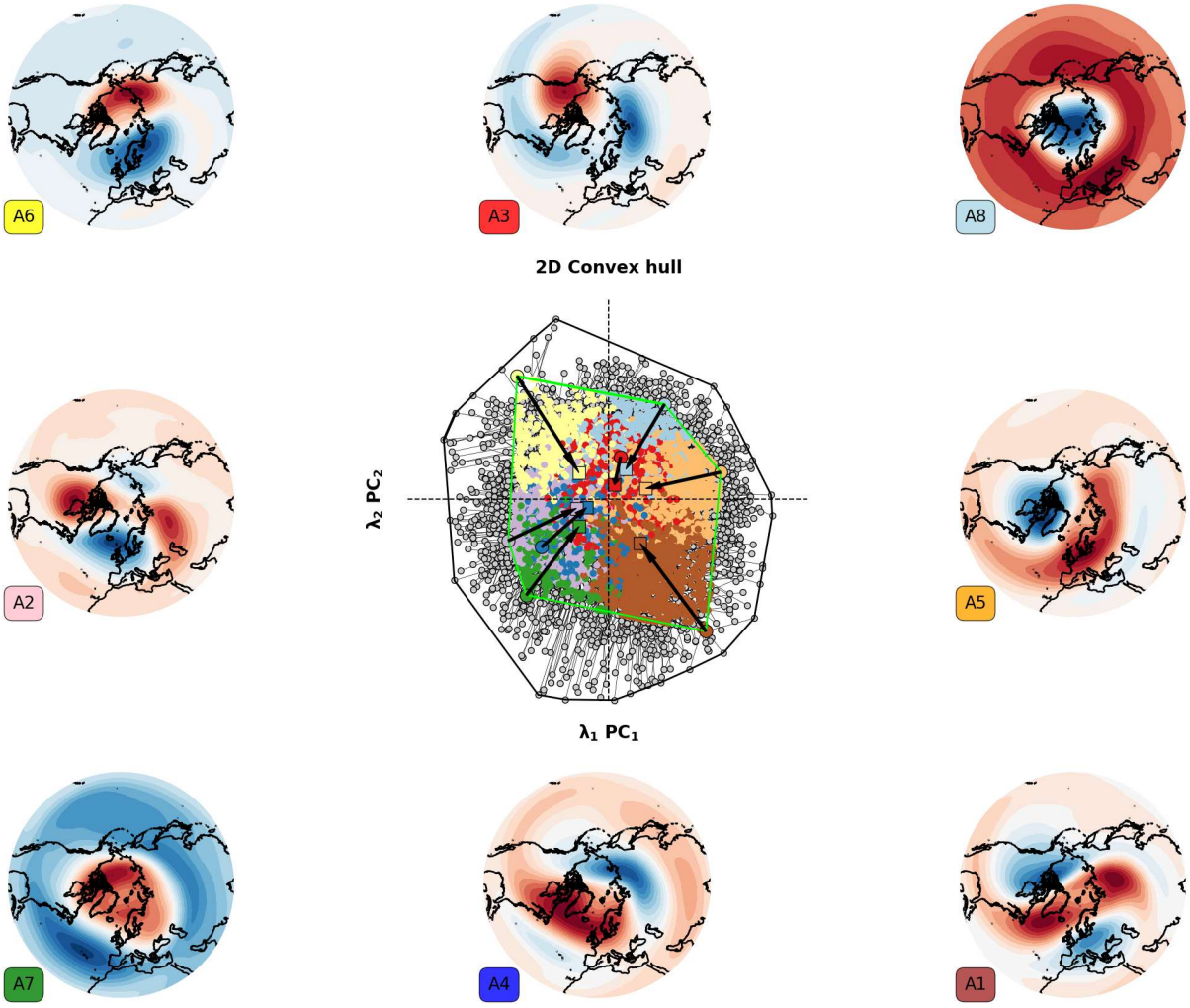

Figure 5: Identified archetypes labeled A1 to A8. They surround the central plot illustrating the dataset with a full convex hull of the 2D data (PC1, PC2) shown in black line and an approximate hull of the 60 PCs in a green line projected onto the 2D space. The archetypes $\mathbf{Z}$ are shown as big colored dots which make corners of the approximate hull. Each one of them shows a different state of vortex. The squares in the central panel represent $\mathbf{XS}^T$, referred to as duals of the archetypes.

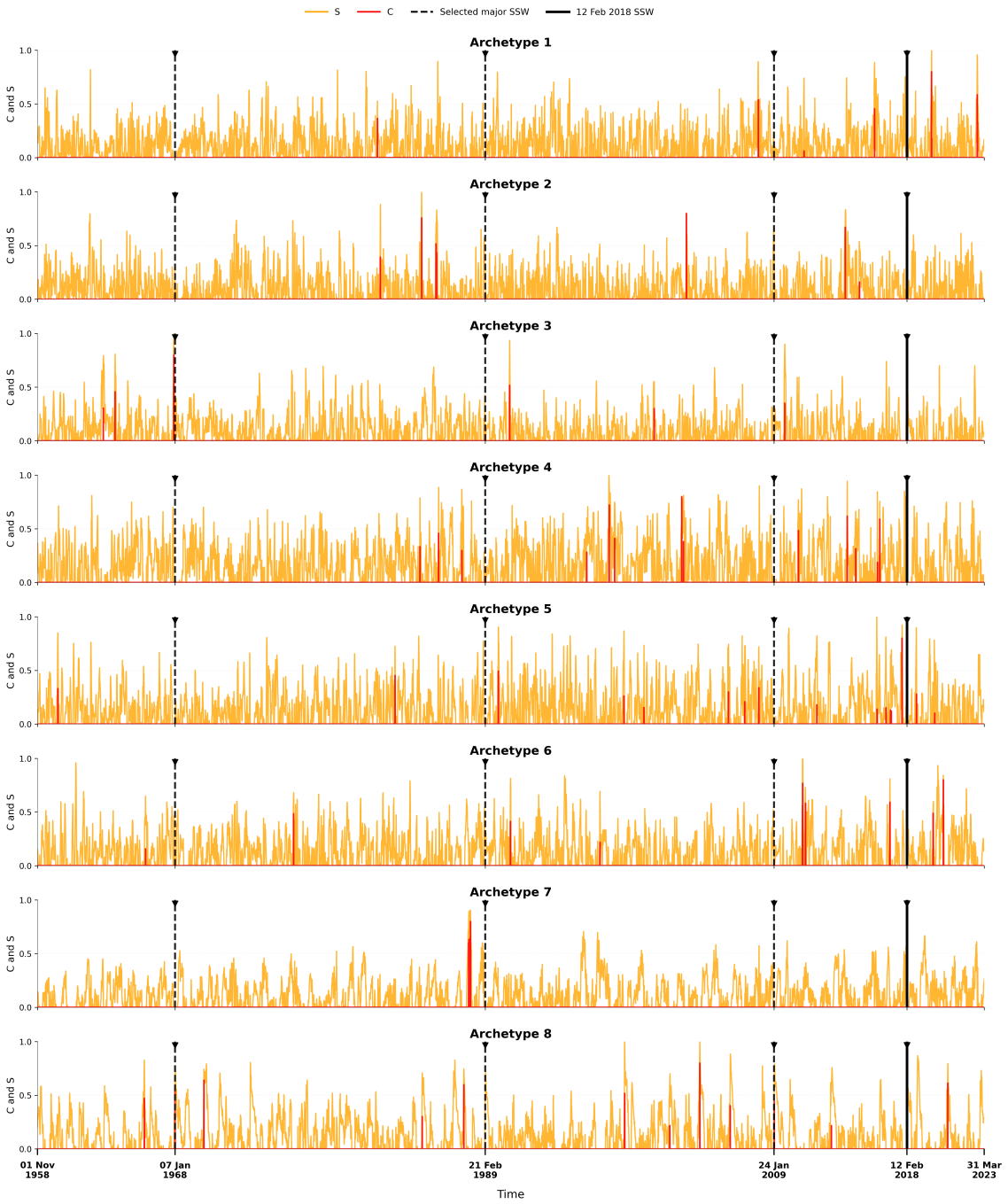

Figure 6: Time series of the weights of **C** (red) and **S** (orange) matrices for the eight identified archetypes. Note that the sum (over time) of the **C**-coefficients is unity (see text) and for visual clarity they have been scaled.

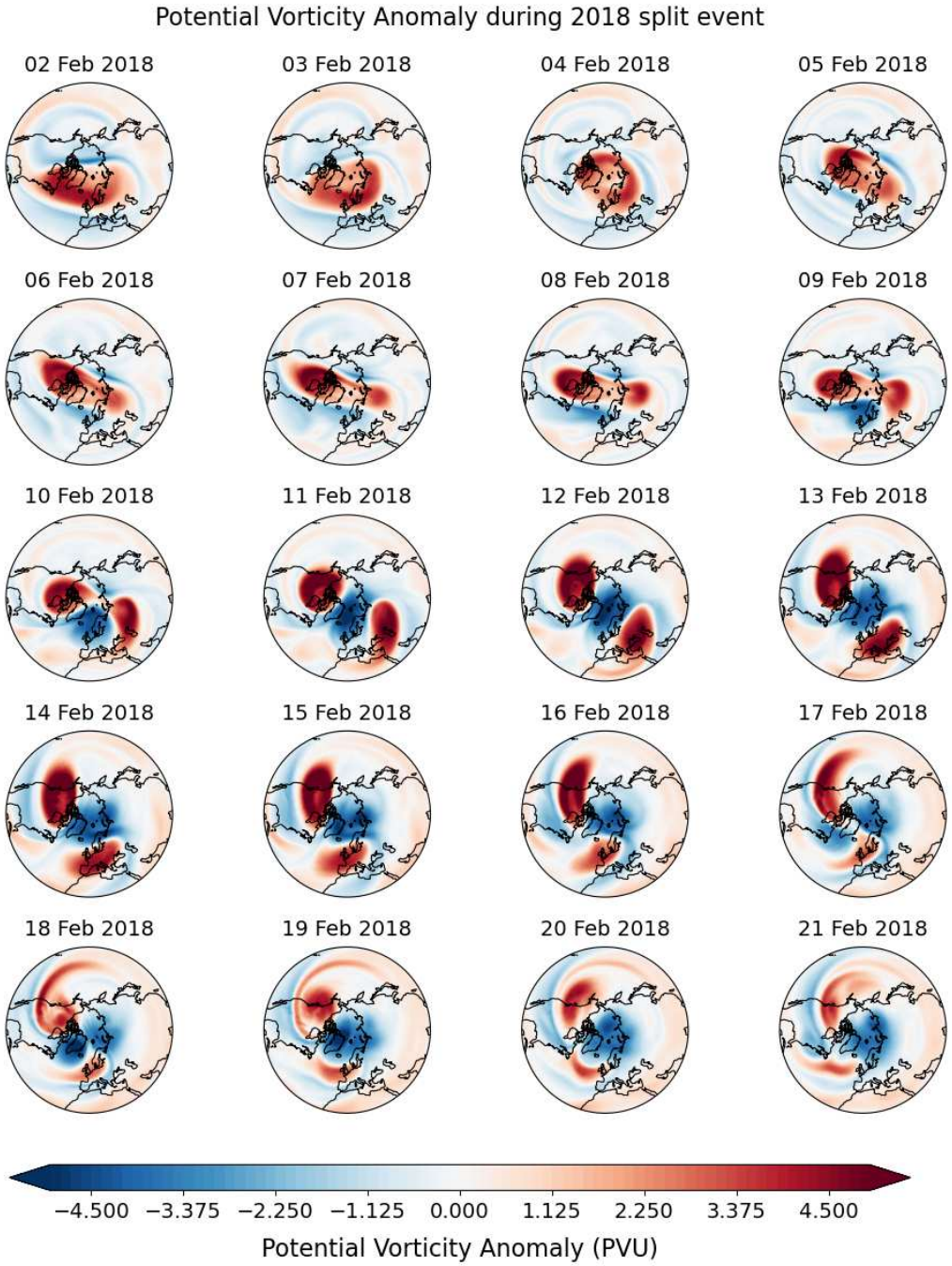

Figure 7: Example of PV evolution for the 2018 event of splitting vortex. The corresponding C weight matrix entry (for A5, Fig. 6) had high values for this particular event (near the end of the record).

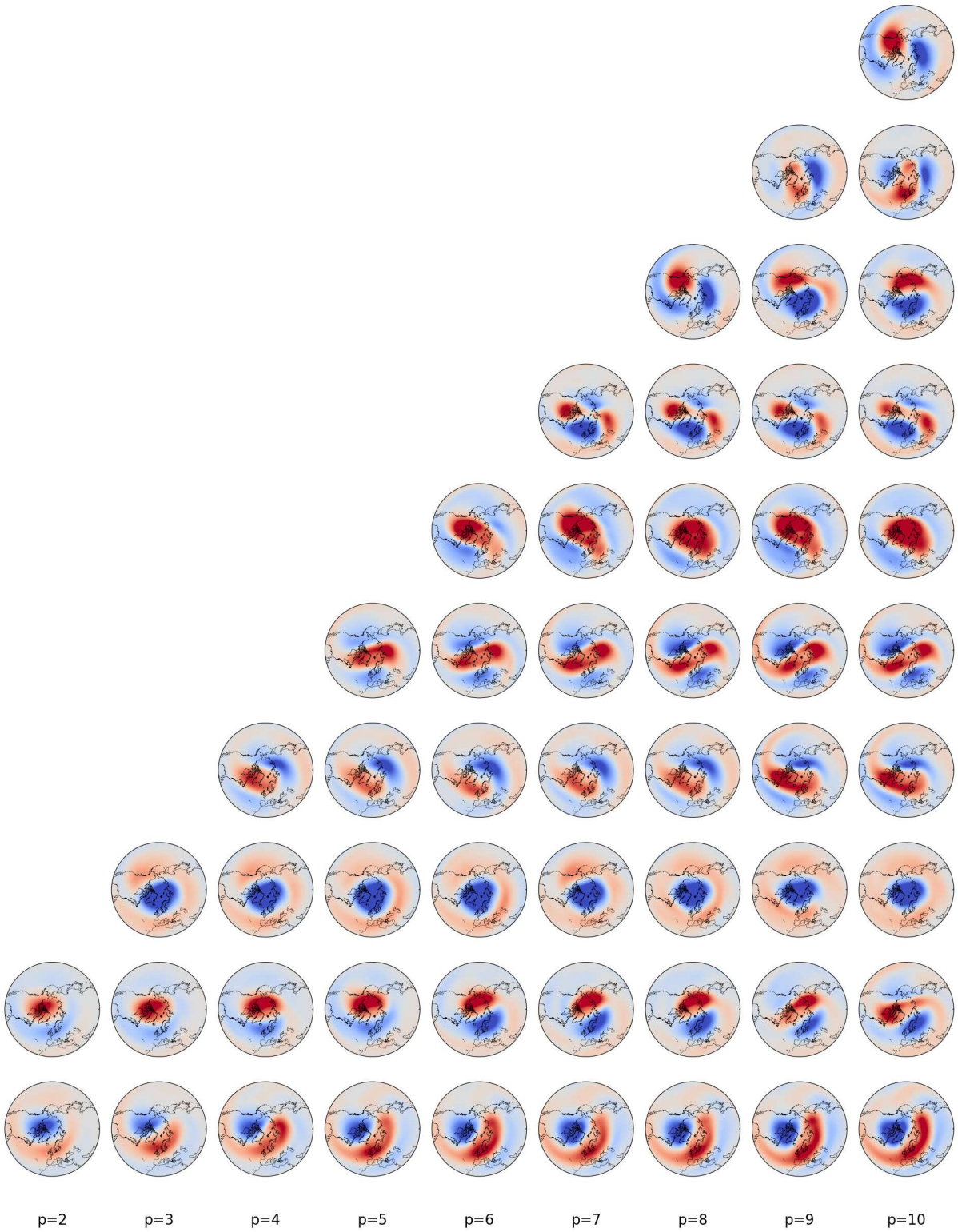

Figure 8: Archetypes of 850K PV anomalies for cardinality ranging from p=2 (left column) to p=10 (right column). The archetypes are arranged based on spatial correlation (rows) reflecting approximate nesting.

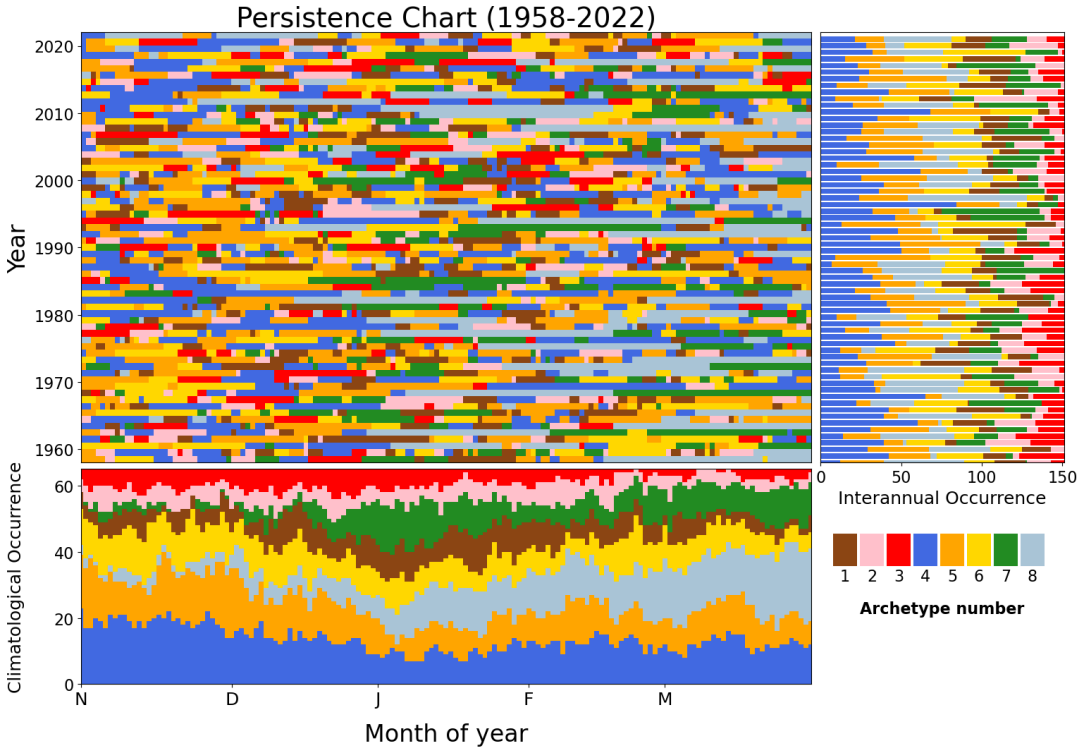

Figure 9: LEGO plot of 850K PV anomalies showing the occurrence frequency (days) of each archetype based on **S**- time series (top left) along with seasonal (bottom) and annual (top right) occurrence.

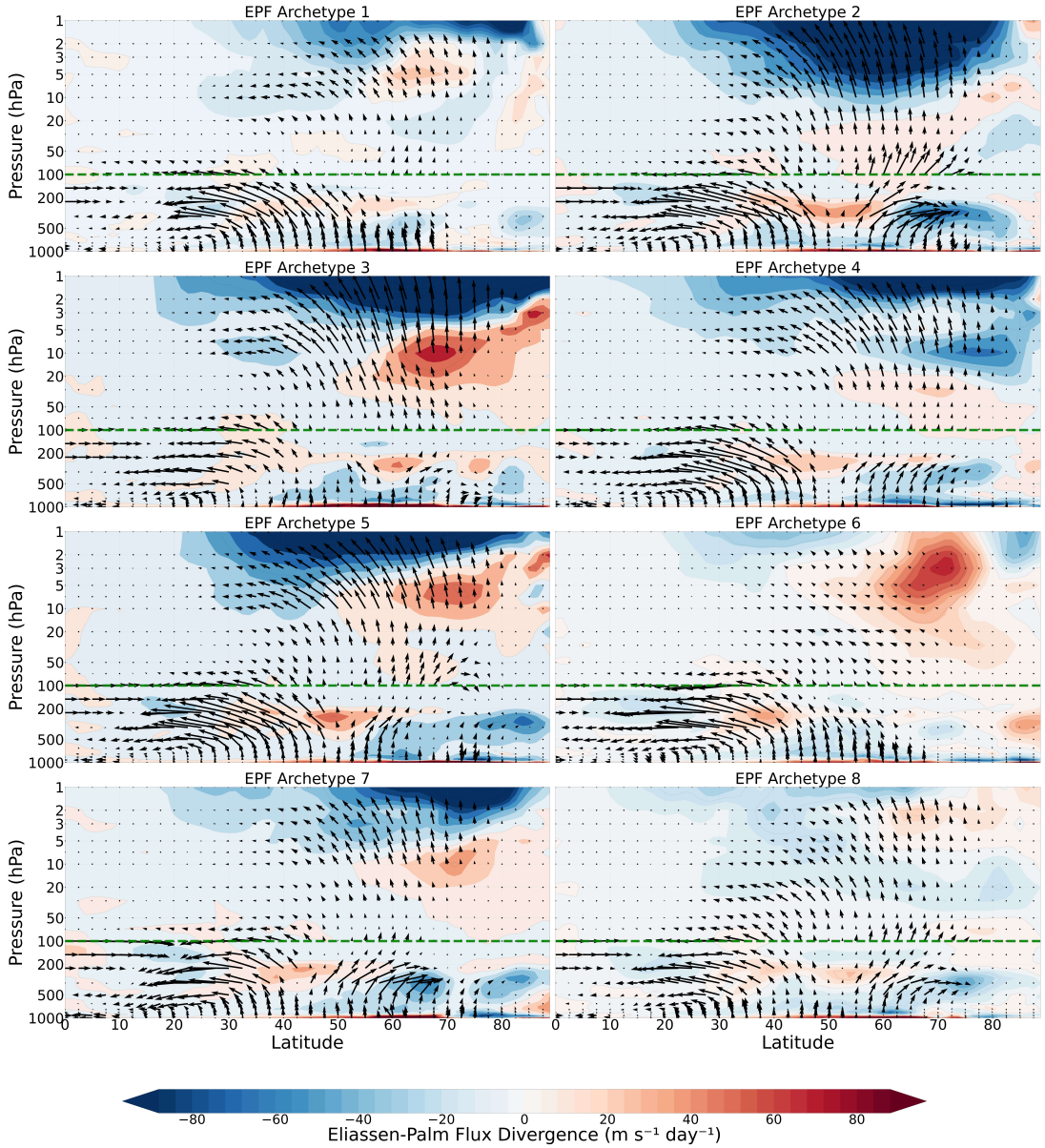

Figure 10: Latitude–height cross sections of Eliassen–Palm (EP) flux and its divergence for the eight C-matrix composites (Archetypes 1–8). Shading denotes EP flux divergence ($ms^{-1}day^{-1}$), with positive (red) and negative (blue) values indicating regions of wave forcing on the mean flow. Arrows show EP flux vectors, scaled separately in the troposphere and stratosphere, with the green dashed line marking the 100 hPa boundary between them. The stratospheric EP flux components are plotted with approximately four times smaller scaling than the tropospheric EP flux components to account for the weaker flux magnitudes aloft. The vertical axis is logarithmic, with a vertical scale factor of 200 applied for visual comparability with the horizontal axis. Divergence fields are uniformly amplified for visual clarity.

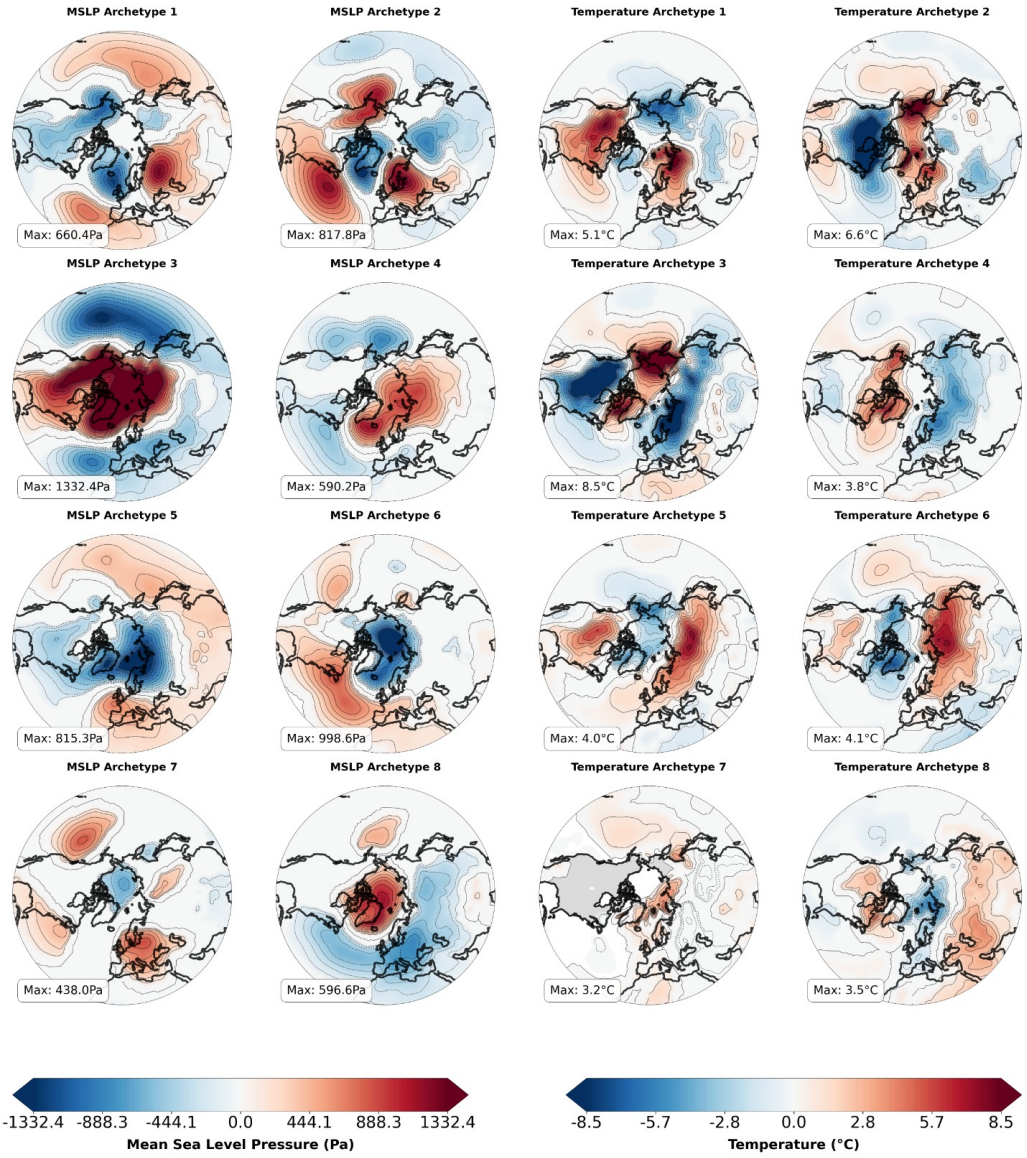

Figure 11: Regression coefficients between **S**-time series of archetypes A1 to A8 and MSLP (first two columns) and surface temperature (last two columns) anomalies. Each subplot shows the maximum value of that variable in the lower right corner. Only significant values (at 5% level) are shown.

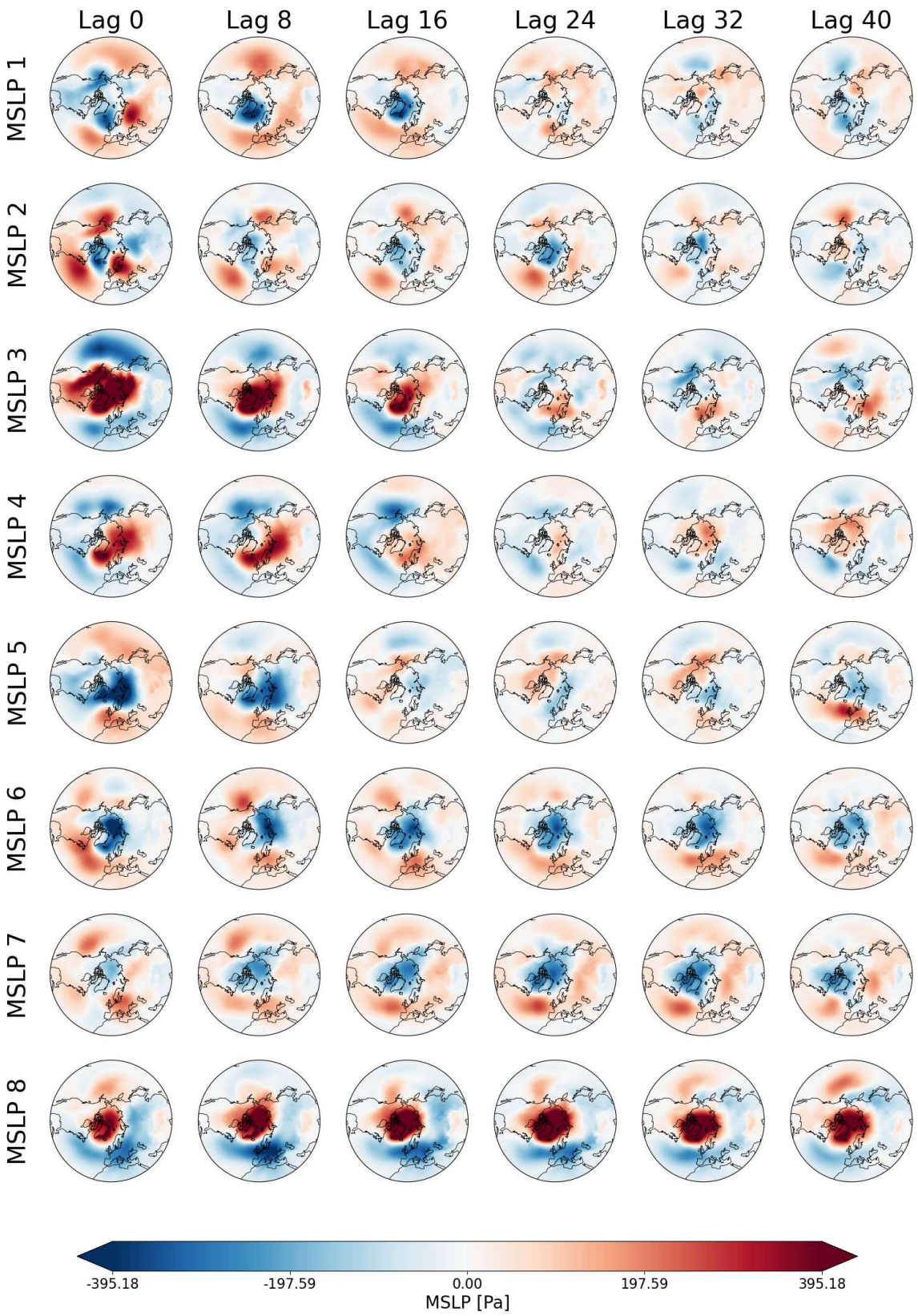

Figure 12: Response of MSLP for different time lags of 8, 16, 24, 32, and 40 days showing regression coefficients between the **S**-time series (leading) and MSLP anomalies (lagging). Columns refer to lags and rows refer to archetypes.

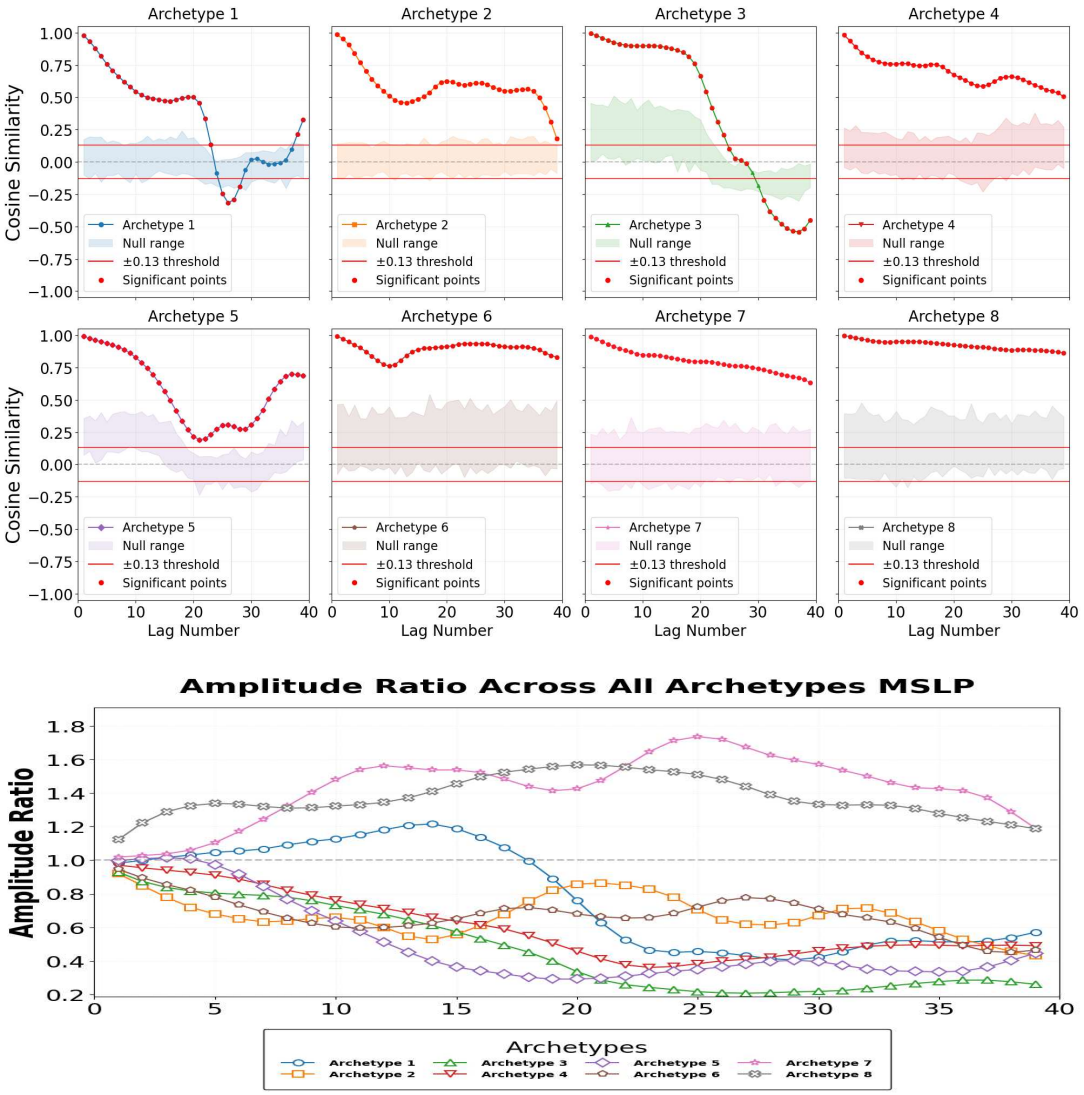

Figure 13: Spatial correlation (top 8 panels) and relative amplitude (bottom panel) for archetypes A1 to A8 MSLP anomaly response (Fig. 12) across different lags (days), see text for details. Horizontal lines and shading show respectively the theoretical (Appendix) and Monte-Carlo 99% confidence levels.

A Appendix Figures

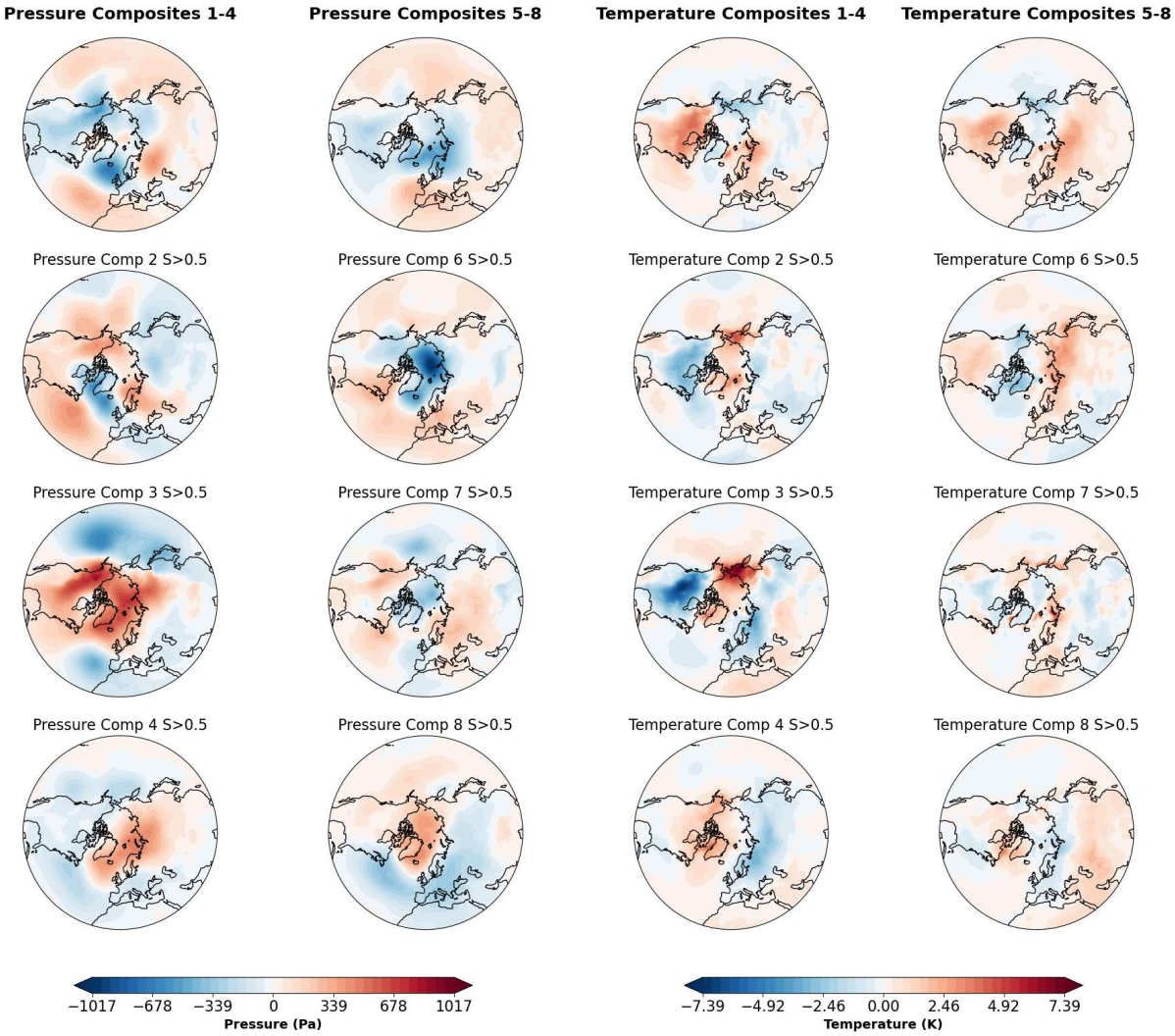

Figure A.1: Anomalous MSLP (first 2 columns) and surface temperature (last two columns) composite based on events when the weight matrix **S** is greater than 0.5 for archetypes A1 to A8

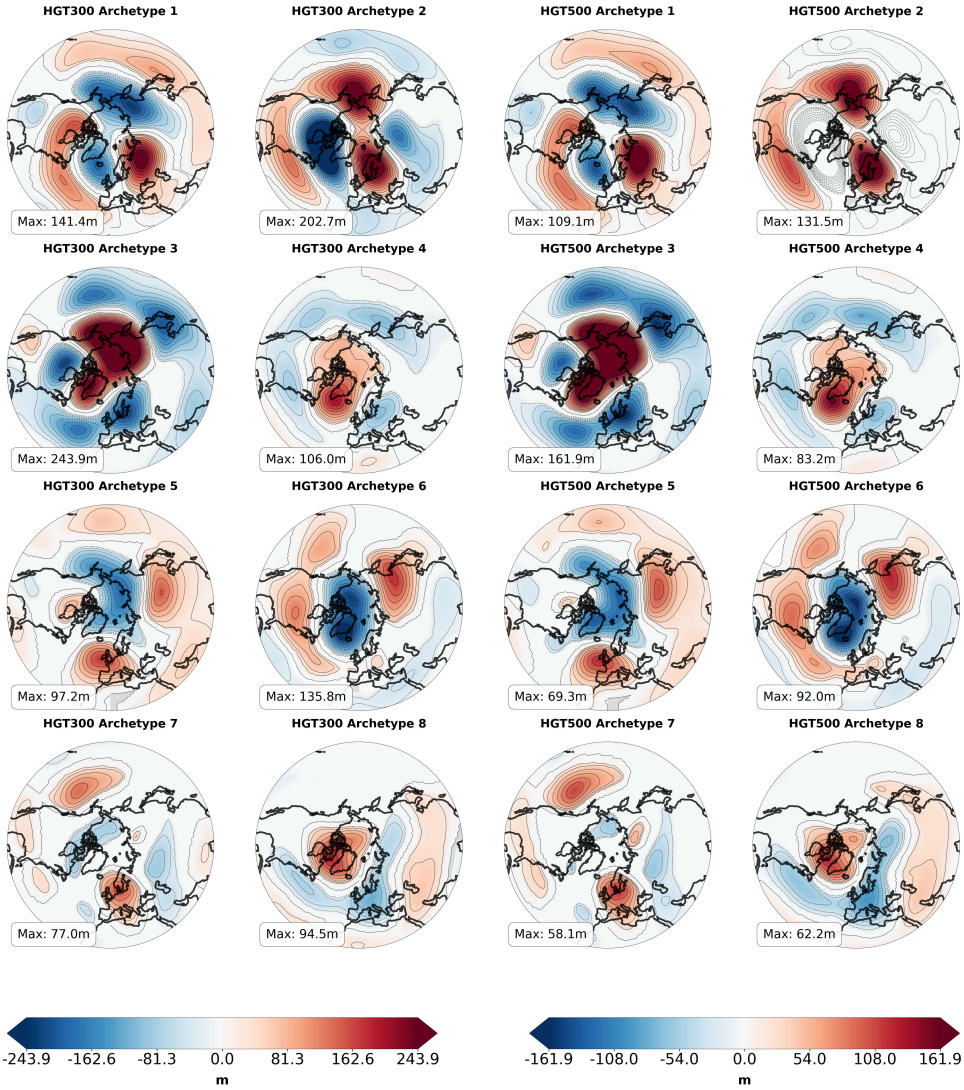

Figure A.2: AS in Fig. 11 but for 300-hPa (first two columns) and 500-hPa (last two columns) anomalies. Only significant values (at 5% level) are shown.

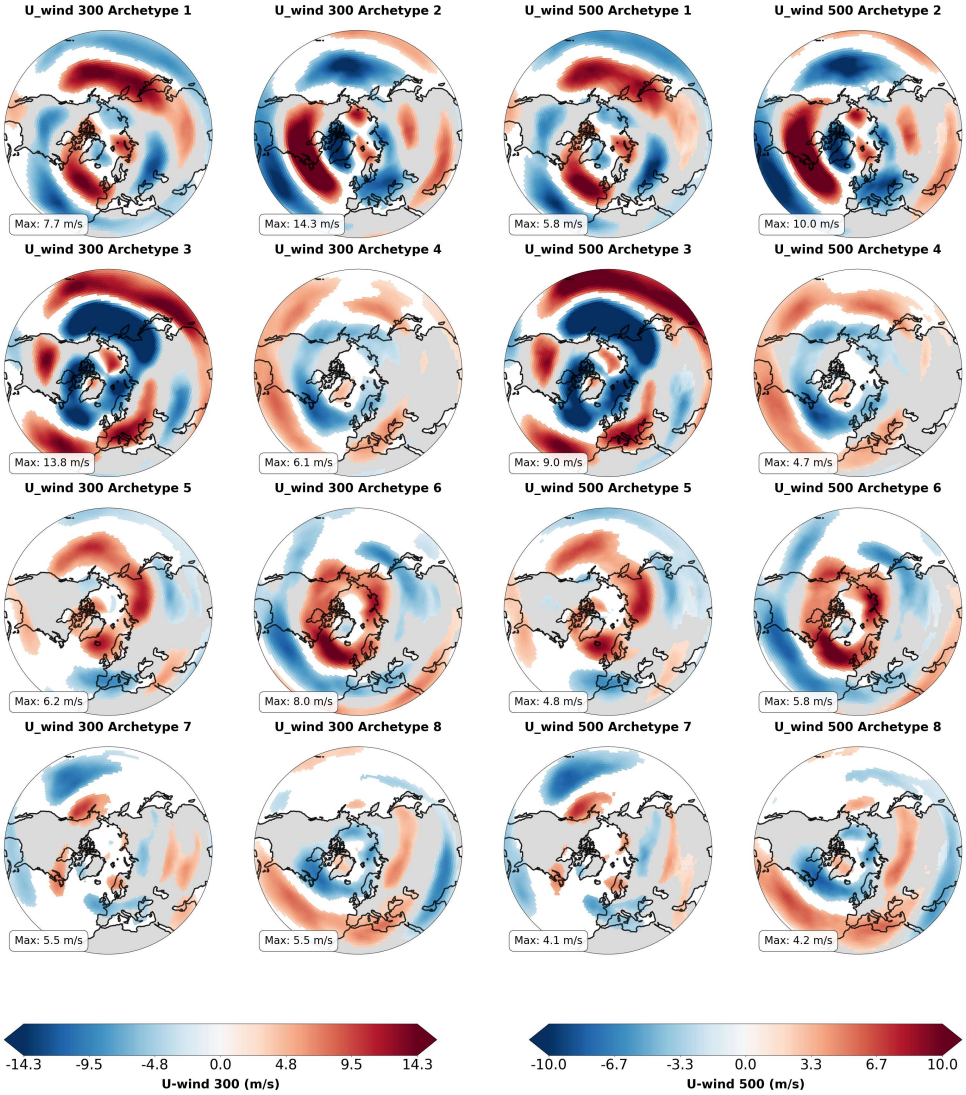

Figure A.3: As in Figure A.2, but for 300-hPa and 500-hPa zonal wind anomalies.

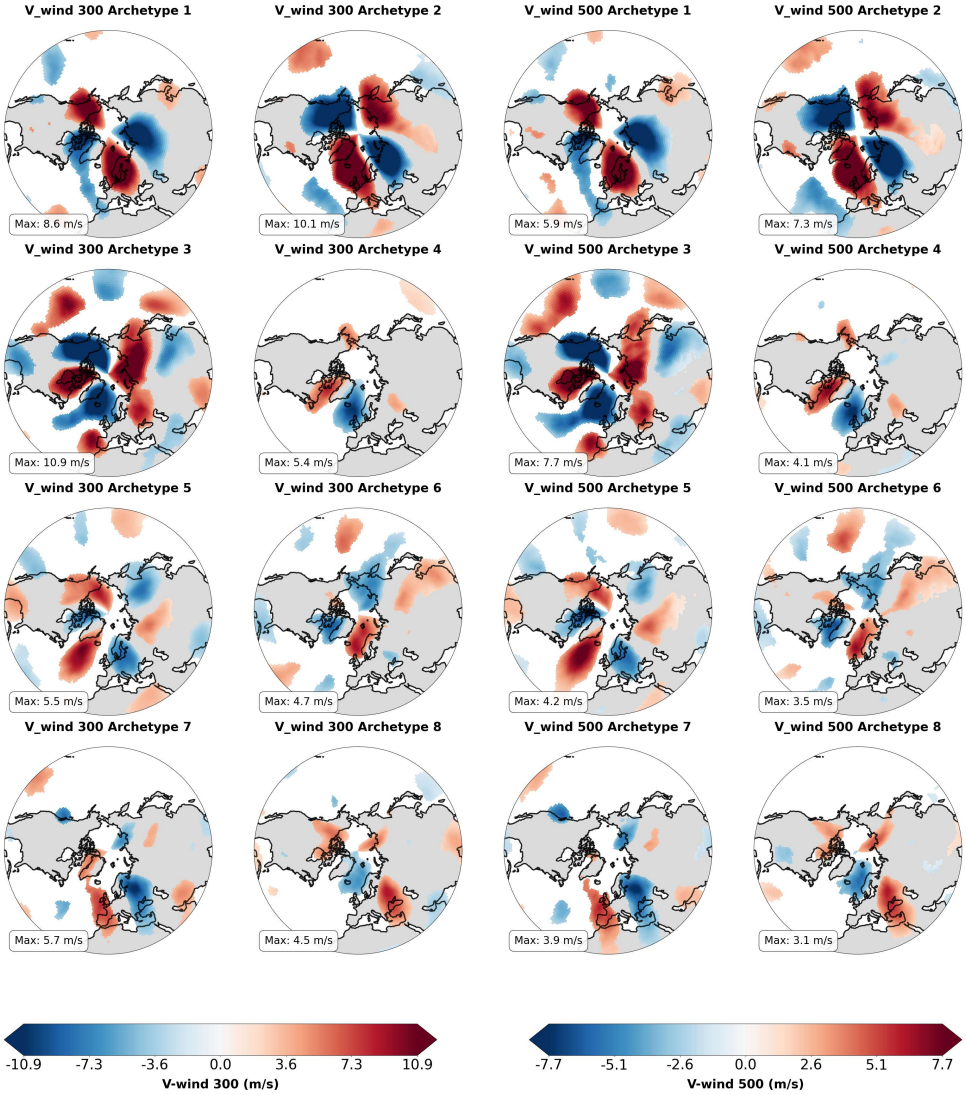

Figure A.4: As in Figure A.3, but for 300-hPa and 500-hPa meridional wind anomalies.

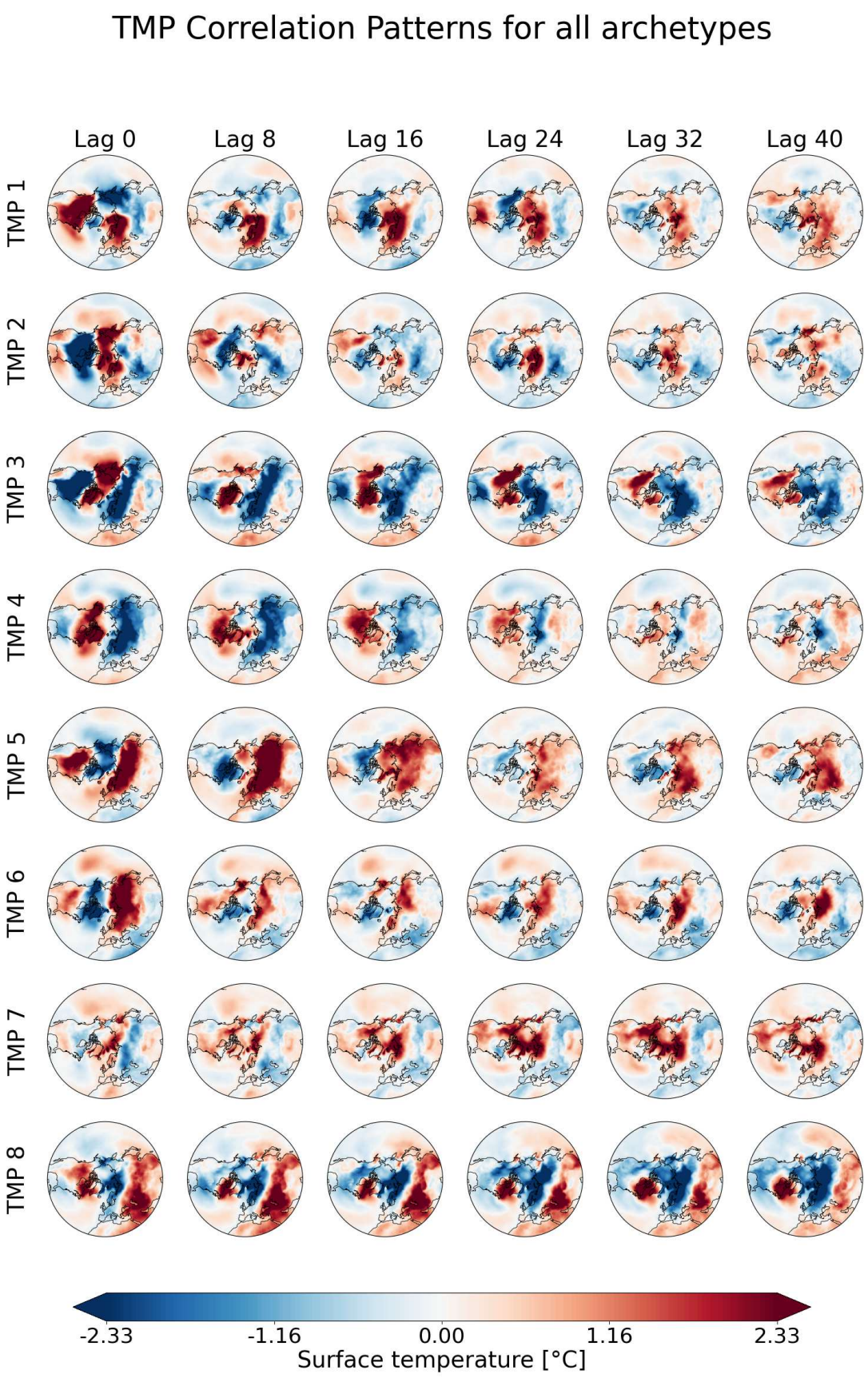

Figure A.5: As in Figure 12 but for the surface temperature anomalies.